



On the grain boundary network characteristics in a martensitic Ti–6Al–4V alloy

Ehsan Farabi¹, Vahid Tari², Peter D. Hodgson¹, Gregory S. Rohrer³, and Hossein Beladi^{1,*}

¹Institute for Frontier Materials, Deakin University, Geelong, VIC 3216, Australia

²Eaton Corporation, Corporate Research & Technology, Southfield, MI 48076, USA

³Department of Materials Science and Engineering, Carnegie Mellon University, Pittsburgh, PA 15213-3890, USA

Received: 25 June 2020

Accepted: 4 July 2020

Published online:

30 July 2020

© Springer Science+Business Media, LLC, part of Springer Nature 2020

ABSTRACT

The characteristics of the intervariant boundary network that resulted from the $\beta \rightarrow \alpha'$ martensitic phase transformation in a Ti–6Al–4V alloy were studied using the crystallographic theories of displacive transformations, five-parameter grain boundary analysis and triple junction analysis. The microstructure of Ti–6Al–4V martensite consisted of fine laths containing dislocations and fine twins. The misorientation angle distribution revealed four distinct peaks consistent with the intervariant boundaries expected from the Burgers orientation relationship. The phenomenological theory of martensite predicted four-variant clustering to have the lowest transformation strain among different variant clustering combinations. This configuration was consistent with the observed Ti–6Al–4V martensitic microstructure, where four-variant clusters consisted of two pairs of distinct V-shape variants. The $63.26^\circ/[\bar{1}055\bar{3}]_{\alpha'}$ and $60^\circ/[11\bar{2}0]_{\alpha'}$ intervariant boundaries accounted for $\sim 38\%$ and 33% of the total population, respectively. The five-parameter boundary analysis showed that the former had a twist character, being terminated on the $(\bar{3}210)_{\alpha'}$ plane, and the latter revealed a symmetric tilt $(10\bar{1}1)_{\alpha'}$ boundary plane. The $63.26^\circ/[\bar{1}055\bar{3}]_{\alpha'}$ and $60^\circ/[11\bar{2}0]_{\alpha'}$ had the highest connectivity at triple junctions among other intervariant boundaries. Interestingly, the boundary network in Ti–6Al–4V martensite was significantly different from the commercially pure Ti martensite, where only $60^\circ/[11\bar{2}0]_{\alpha'}$ intervariant boundaries largely were found at triple junctions due to the formation of three-variant clustering to minimize the transformation strain. This difference is thought to result from a change in the martensitic transformation mechanism (slip vs twinning) caused by the alloy composition.

Address correspondence to E-mail: hossein.beladi@deakin.edu.au

Introduction

The evolution of the grain boundary network in titanium alloy during processing influences material performance [1]. Grain boundary crystallography (i.e. lattice misorientation and grain boundary plane orientation) impacts a boundary resistance to dislocation motion [2–5] and slip transfer character [6, 7]. Therefore, the optimization of the grain boundary network with respect to the population and connectivity of the boundary of interest can further enhance the properties in the polycrystalline materials [8, 9]. In this regard, tailoring the grain boundary character and network to improve material performance has been a topic of considerable research. For example, it has been found that the characteristics of the grain boundary are influenced by different parameters such as chemical composition [10–13], crystal structure [14–16], thermomechanical processing [17–23] and phase transformation paths/mechanisms [24, 25].

There have been many studies that show how thermomechanical processing [17–22, 25, 26] and/or specific phase transformation paths [27, 28] can be used to engineer the grain boundary network. While the thermomechanical processing changes the character of the grain boundary network through activation of particular restoration processes during the deformation and subsequent annealing treatment, the occurrence of phase transformation abolishes the high-temperature microstructure and develops a unique grain boundary network. Therefore, the latter can be considered as an effective apparatus for engineering of the grain boundary network of metals undergoing phase transformation (e.g. steels and Ti alloys). Significant studies have been conducted on steels, demonstrating that the competition between the phase transformation mechanisms (shear vs diffusion) upon the austenite (FCC) to ferrite (BCC) transformation can significantly alter the grain boundary network (i.e. character, population and connectivity) [15, 25, 27–32]. It was concluded that the crystallographic orientation relationship between austenite and ferrite, and the occurrence of variant selection (i.e. frequent appearance of some variants than the others) during phase transformation should be considered as a major factor to engineer the grain boundary network.

Unlike steels, there are fewer studies of grain boundary network evolution in Ti alloys undergoing $\beta(\text{BCC}) \rightarrow \alpha(\text{HCP})$ phase transformation upon cooling [24, 33, 34]. Here, the phase transformation is closely governed by the well-known Burgers orientation relationship (OR) [35], leading to the formation of up to 12 crystallographically distinct α variants from a given β parent grain. Interestingly, the microstructure characteristics of the Ti alloys are strongly dependent on the active transformation mechanism (i.e. shear vs diffusion), which may lead to a preferred α variant/s formation (i.e. variant selection) [28–39]. Therefore, the control of dominant variant arrangement/selection can significantly affect the transformed texture and the α/α boundaries that result from the $\beta \rightarrow \alpha$ transformation in Ti-alloys.

During the martensitic/shear transformation, the nucleation of a martensitic variant requires the lattice invariant shear to be fulfilled through either slip and/or twinning mechanisms, depending on the lattice parameters of parent (i.e. a_β) and transformed product (i.e. $a_{\alpha'}$ and $c_{\alpha'}$) [40]. Furthermore, the elastic strain fields developed during the nucleation of a martensitic α' variant interact with other variants in a way that a total reduction in the strain energy for the cluster of variants is achieved [33, 34, 40–44]. This results in distinct morphologies, namely the diamond-shape [45–47] and/or triangular morphology [33, 34, 44, 47]. The phenomenological theory of the martensitic/displacive transformation was widely used to identify the strain energy associated with the variant formation during martensitic transformation. It was demonstrated that the shape strain can be accommodated by forming a three-variant arrangement where dislocation slip is the dominant mechanism during Ti martensite transformation (e.g. commercially pure Ti). Such variant assembly has resulted in an increase in the twin-related $60^\circ/[1\ 1\ \bar{2}0]$ intervariant boundaries. In parallel, the local stress induced by the formation of the primary α' lath can lead to the nucleation of closely orientated α' variants [48–51]. Although similar approaches were applied to define the self-accommodating cluster characteristics, however, the role of the martensite transformation mechanism (i.e. slip vs twinning) on the dominant self-accommodation morphology and the resultant intervariant boundary network (i.e. α'/α' boundaries resulted from the $\beta \rightarrow \alpha'$ transformation) in Ti alloys is not fundamentally understood.

The aim of the current study was to establish an understanding of the variant arrangement development and the resultant intervariant boundary network characteristics (α'/α' boundaries resulted from the $\beta \rightarrow \alpha'$ transformation) during the martensitic transformation of Ti–6Al–4V that minimizes the transformation strain, when twinning is the dominant martensitic phase transformation mechanism. To this end, the phenomenological theory of the martensite transformation, as explained by Wechsler, Liberman and Read (WLR) [52–54], was used to predict the morphological arrangement of the possible α variants in the martensitic Ti–6Al–4V alloy. Furthermore, the intervariant boundary characteristics were studied using a stereological interpretation of conventional EBSD maps along with five-parameter crystallographic analysis [21]. This approach made it possible to measure the grain boundary plane distribution for all of the intervariant boundaries. Finally, the connectivity of the intervariant boundaries was analysed by classifying triple junctions according to the number of intervariant boundaries that meet at a junction. These findings ultimately make it possible to propose a mechanism for intervariant network formation in Ti alloys formed through phase transformation and engineer the microstructure with an optimum intervariant boundary network for a specific application.

Experimental

Material and heat treatment procedure

A hot-rolled Ti–6Al–4V alloy with a composition of Ti–6.05 Al, 3.98 V (in wt%) was used for the current study. A rectangular sample with dimensions of 60 mm \times 30 mm \times 10 mm was prepared from the hot-rolled plate, where the longest length was aligned with the rolling direction. The sample was then coated by the delta glaze coating to prevent high-temperature oxidation. The Ti–6Al–4V sample was heated up to 1100 °C using a servo-testing machine. The sample was held isothermally for 3 min at the corresponding reheating temperature to obtain a fully β microstructure with a grain size of \sim 250 μ m. Then, the sample was immediately water-quenched to room temperature, resulting in a fully martensitic microstructure. The constituent phases of the as-received and processed Ti–6Al–4V alloy were

measured using a PANalytical X-ray diffractometer. The machine setting for the measurements was at the voltage of 40 kV and current of 30 mA, respectively. The constituent phases were analysed using the point scan settings with 0.02° step size and time per step of 5.

Microstructural characterization

The microstructure of the samples was studied by scanning electron microscopy (SEM), electron backscatter diffraction (EBSD), transmission Kikuchi diffraction (TKD) and transmission electron microscopy (TEM). For the EBSD, the as-received sample was ground and polished using a 0.04 μ m OPS suspension. The EBSD measurement for the as-received sample was performed using a FEG Quanta 3-D FEI SEM with the beam operated at 20 kV and 8 nA. The martensitic microstructure formed in the Ti–6Al–4V alloy was too fine to employ the conventional EBSD technique. Hence, the TKD technique was utilized for the Ti–6Al–4V martensitic microstructure analysis. For the TKD analysis of the Ti–6Al–4V alloy, thin foil samples with a thickness of 70 μ m were prepared similar to the transmission electron microscopy (TEM) sample preparation routine. The thin foils were twin-jet electropolished by A3 Struers™ electrolyte solution containing 6% perchloric acid and 35% butoxymethanol and 64% methanol at -40 °C using a potential of 35 V. It should be noted that the texture bias in the grain boundary characterization was reduced through conducting TKD on two perpendicular cross sections (e.g. parallel and perpendicular sections with respect to the rolling direction). A similar procedure was employed to prepare TEM samples.

The TKD measurements were conducted by a FEG Quanta 3-D FEI SEM instrument under 30 kV and 8 nA conditions using the Oxford Instruments TKD sample holder. TSL software was employed to acquire the TKD data using a hexagonal grid with a step size of 0.5 μ m and 10 nm for the as-received and martensitic sample, respectively. Multiple TKD scans on a total area of 1296 μ m² (i.e. 36 μ m \times 6 μ m \times 6 μ m) were executed on the martensitic microstructure. To avoid collecting multiple boundary data from a given prior β grain, only two TKD maps with a distance of at least 250 μ m were acquired from each thin foil. Moreover, the data were acquired equally from both RD-TD and ND-TD cross sections of the sample

to compensate the texture effect on the five-parameter grain boundary characterization. Therefore, multiple thin foils were prepared to accommodate several prior β grains from different sections of the transformed sample for TKD data acquisition.

The TKD post-processing was conducted using the TexSEM Laboratories Inc., software (TSL). In parallel, the TEM examination of thin foils of the Ti–6Al–4V alloy was conducted using a JEM 2100 microscope operated at 200 kV.

Intervariant boundary analysis

A stereological analysis, which has been fully described in previous studies [55, 56], was employed to identify the interviant boundary plane distribution in the martensitic microstructure. Before extracting the boundary segments from the TKD maps, a multiple-step cleaning procedure was considered. First, the ambiguous data were removed through the grain dilation function. Then, a single average orientation was assigned to the neighbouring groups of pixels with a disorientation angle of less than 5° (one single grain). Pseudo-symmetry of the Kikuchi patterns misoriented by $30^\circ/[11\bar{2}0]_{\alpha'}$ was also cleaned from the obtained data. This was followed by cleaning of data points having a confidence index of less than 0.1. The effect of each cleaning step on the TKD data is illustrated in the supplemental Figure S1. To extract the boundary line traces/segments from the TKD data, the reconstructed grain boundary function with a boundary deviation limit of 2 pixels (e.g. 20 nm for Ti–6Al–4V martensite) [57] was used. Here, a total of $\sim 107,000$ boundary line traces was extracted from the TKD maps for the martensitic microstructure of Ti–6Al–4V. For materials with a hexagonal crystal structure, at least 200,000 boundary line traces are required to reliably analyse the boundary plane orientation. However, due to the crystallographic constraints associated with the martensitic transformation in Ti alloys, the boundaries revealed a few nearly discrete misorientations (rather than being spread over all possibilities). Therefore, it is possible to reliably measure the grain boundary plane orientation distribution at these specific misorientations with a smaller number of boundary line segments (i.e. $\sim 100,000$ boundary segments). After extracting the line segments, the stereological procedure was applied to calculate the five-parameter grain boundary character distribution

(GBCD). Through this approach, the grain boundary plane character distribution was identified at different grain boundary misorientations. The measurement was conducted with 9 bins per 90° , providing 10° resolution.

Results

The evolution of microstructure in martensite transformation

Microstructure

The as-received microstructure of the Ti–6Al–4V alloy had a typical rolled microstructure consisting of elongated α and β phases (Fig. 1a). The presence of both α and β phases in the as-received microstructure was also observed in the related XRD pattern of the Ti–6Al–4V alloy (Fig. 1b). The heat treatment procedure for the Ti–6Al–4V alloy resulted in a very fine and fully martensitic microstructure (i.e. an average lath thickness of $\sim 0.43 \pm 0.01 \mu\text{m}$, Fig. 2a), having no sign of remaining β phase, as observed through the XRD measurement (Fig. 2b). The parallel lines appeared in Fig. 2a are artefacts associated with the instability of electron beam during the TKD experiments. These lines were ignored as they had minimal effect on the grain boundary network characterization. The bright-field TEM examination also revealed fine martensitic laths with a dislocation substructure along with very thin transformation twins (highlighted by an arrow in Fig. 3). These twins were mostly separated by $60^\circ/[11\bar{2}0]_{\alpha'}$ (shown by yellow box in Fig. 2a). It should be noted that the transformation twins observed in TEM images have been partially indexed by the TKD, which appeared to be parallel or perpendicular to the interviant boundaries (Fig. 3). Using the trace analysis, both types of twins showed a $(10\bar{1}1)_{\alpha'}$ plane orientation (see Fig. S2 in the supplementary information section).

The Ti–6Al–4V alloy also revealed distinct morphological arrangements of α' laths. Here, two different arrangements were observed, namely the V-shape morphology due to the impingement of two distinct variants, and the quadrilateral configuration consisting of four distinct variants (highlighted by red box in Fig. 2a). The remaining space within these microstructure configurations was filled with smaller V or quadrilateral morphological features (Fig. 2a).

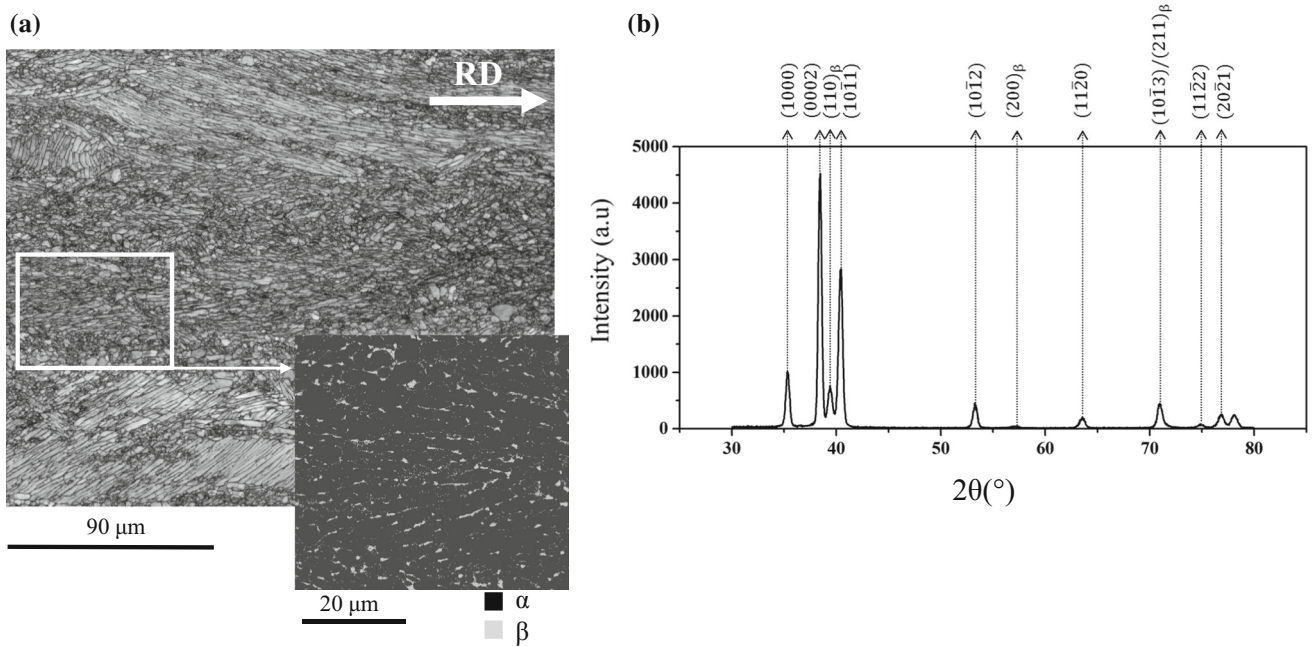


Figure 1 (a) The band contrast image and phase map of the as-rolled Ti-6Al-4V alloy, and (b) the corresponding XRD pattern revealing both α and β phase peaks.

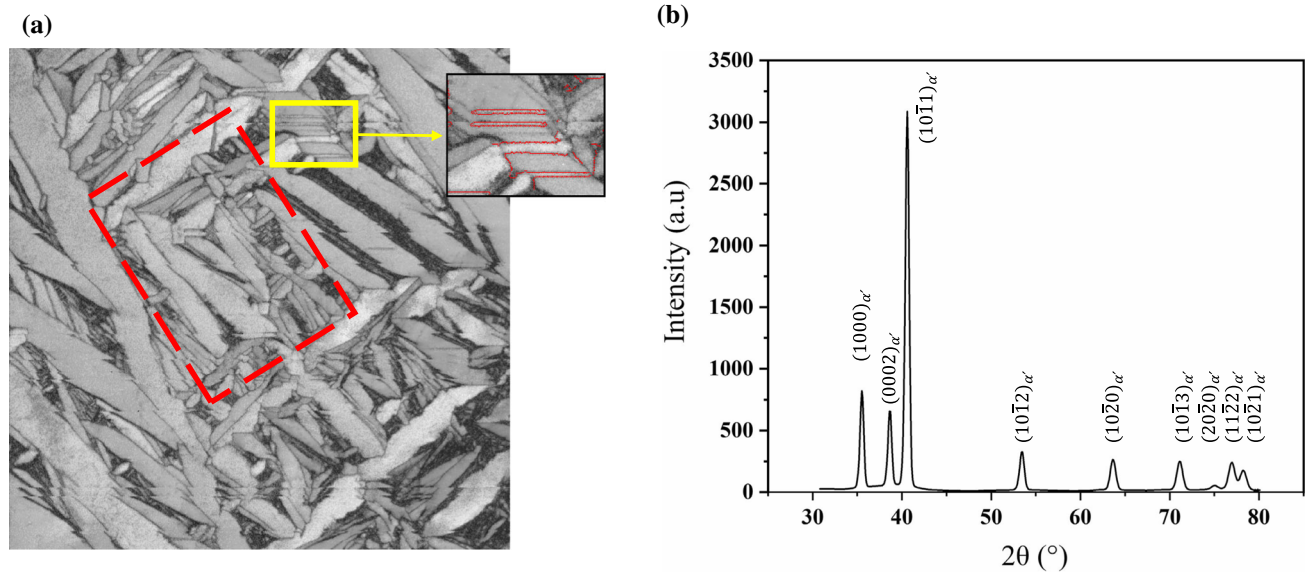


Figure 2 (a) The Kikuchi pattern quality map of the martensitic microstructure in the Ti-6Al-4V alloy, (b) the corresponding XRD pattern revealing only α phase in the microstructure. The red lines in (a) represent $60^\circ/[11\bar{2}0]_\alpha$ grain boundaries.

The martensite intervariant boundary plane character distribution

The misorientation angle distribution of the martensitic microstructure for the Ti-6Al-4V alloy showed multiple peaks at the positions of $\sim 10^\circ$, $55\text{--}65^\circ$ and $\sim 90^\circ$ (Fig. 4a), significantly different from what

is expected for a random distribution. The misorientation axis distribution associated with each peak was clustered at a specific axis. The misorientation axes were close to what is expected from the Burgers OR which were introduced in the work of Gey et. al [58]. (Table 1). The points with non-ideal axes can arise from the intersection of alpha variants from different

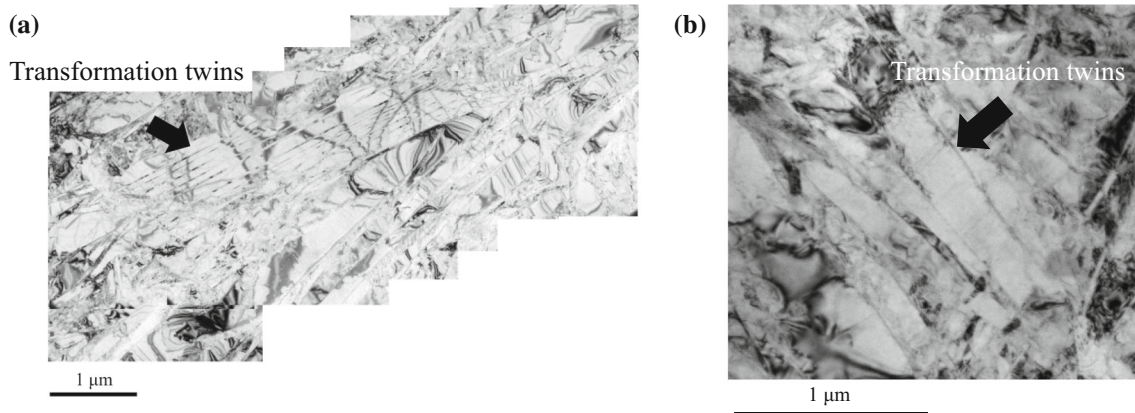


Figure 3 The TEM bright-field micrograph of the martensitic α laths in Ti-6Al-4V alloy including (a) twins parallel and (b) perpendicular to the martensite laths.

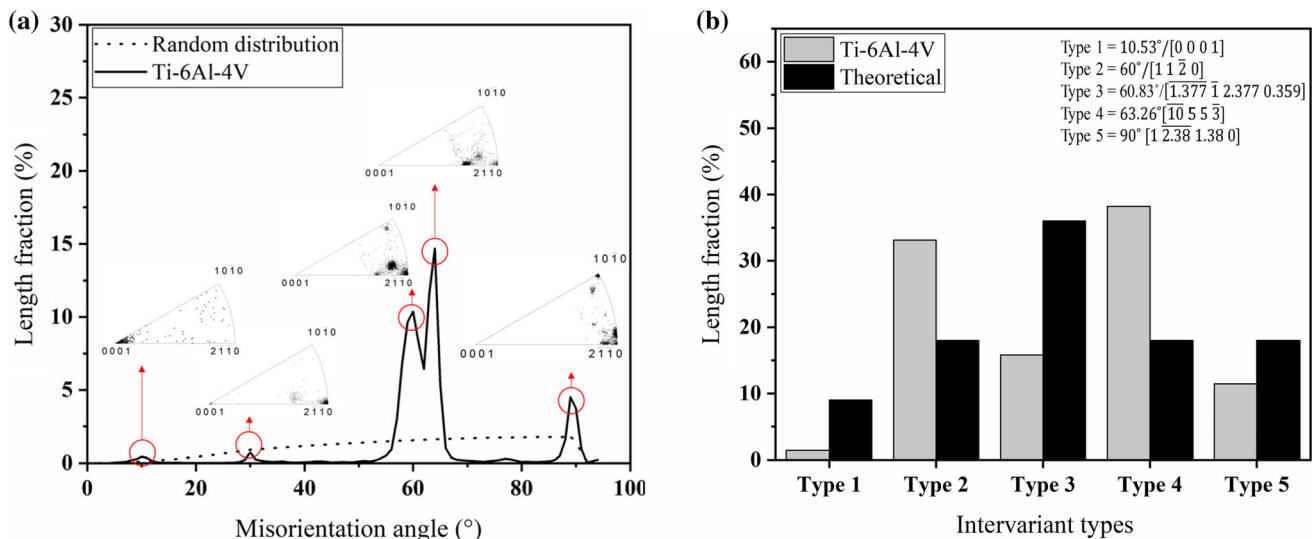


Figure 4 (a) The misorientation angle distribution of martensitic microstructure in Ti-6Al-4V alloy, and (b) the length fraction of intervariant boundaries associated with Burgers orientation

prior β grains or from boundaries that fall within the misorientation angle tolerance. As illustrated in supplemental Figure S3, the number of non-ideal points decreases with a smaller tolerance angle. The $\sim 63^\circ$ misorientation angle had the highest population, while the $\sim 10^\circ$ had the lowest intensity in the misorientation angle distribution profile. The boundaries responsible for the peak near 30° are disoriented about the $[11\bar{2}0]_{\alpha'}$ axis, which is consistent, within experimental resolution, with a symmetric tilt grain boundary at 31.4° that calculations predict has a low grain boundary energy [59]. Here, the grain boundaries associated with the Burgers OR

relationship. The theoretically calculated fractions are based on the assumption that all variants have equal statistical probability during the phase transformation.

were only examined, and the $30^\circ/[11\bar{2}0]_{\alpha'}$ was not further considered.

Figure 4b compares the theoretical fraction of intervariant boundaries formed through the ideal Burgers OR with the experimental results obtained from the martensitic microstructure in Ti-6Al-4V. The spatial distribution of the boundaries with the Burgers OR, in a single orientation map, is illustrated in supplemental Figure S4. Here, the theoretical distribution of intervariant boundaries was calculated considering that all variants occur in the product phase with an equal probability. The most common intervariant boundary for the Ti-6Al-4V alloy was the $63.26^\circ/[\bar{1}055\bar{3}]_{\alpha'}$ boundaries having $\sim 38\%$ of

Table 1 Individual variants of Burgers OR corresponding to the β matrix and the α product phase [58]

Variants	Orientation relationship	Intervariant boundary (from V_1)
1	$(1\bar{1}0)_\beta // (0001)_\alpha, [111]_\beta // [11\bar{2}0]_\alpha$	–
2	$(10\bar{1})_\beta // (0001)_\alpha, [111]_\beta // [11\bar{2}0]_\alpha$	$[11\bar{2}0]/60^\circ$
3	$(01\bar{1})_\beta // (0001)_\alpha, [111]_\beta // [11\bar{2}0]_\alpha$	$[11\bar{2}0]/60^\circ$
4	$(110)_\beta // (0001)_\alpha, [\bar{1}11]_\beta // [11\bar{2}0]_\alpha$	$[1\bar{2}.38\bar{1}.380]/90^\circ$
5	$(101)_\beta // (0001)_\alpha, [\bar{1}11]_\beta // [11\bar{2}0]_\alpha$	$[\bar{1}055\bar{3}]/63.26^\circ$
6	$(01\bar{1})_\beta // (0001)_\alpha, [\bar{1}11]_\beta // [11\bar{2}0]_\alpha$	$[\bar{1}.377\bar{1}2.3770.359]/60.83^\circ$
7	$(110)_\beta // (0001)_\alpha, [1\bar{1}1]_\beta // [11\bar{2}0]_\alpha$	$[1\bar{2}.38\bar{1}.380]/90^\circ$
8	$(10\bar{1})_\beta // (0001)_\alpha, [1\bar{1}1]_\beta // [11\bar{2}0]_\alpha$	$[\bar{1}.377\bar{1}2.3770.359]/60.83^\circ$
9	$(011)_\beta // (0001)_\alpha, [1\bar{1}1]_\beta // [11\bar{2}0]_\alpha$	$[\bar{1}055\bar{3}]/63.26^\circ$
10	$(1\bar{1}0)_\beta // (0001)_\alpha, [11\bar{1}]_\beta // [11\bar{2}0]_\alpha$	$[0001]/10.53^\circ$
11	$(101)_\beta // (0001)_\alpha, [11\bar{1}]_\beta // [11\bar{2}0]_\alpha$	$[\bar{1}.377\bar{1}2.3770.359]/60.83^\circ$
12	$(011)_\beta // (0001)_\alpha, [11\bar{1}]_\beta // [11\bar{2}0]_\alpha$	$[\bar{1}.377\bar{1}2.3770.359]/60.83^\circ$

total boundary length, though the $60^\circ/[11\bar{2}0]_\alpha$ intervariant had the second highest population with $\sim 33\%$ of total boundary length. On the other hand, the $10.53^\circ/[0001]_\alpha$ intervariant was the least common boundary, consuming about 1% of all boundary length. The other intervariant boundary length fractions in the martensitic Ti–6Al–4V were $\sim 16\%$ and 11% for $60.83^\circ/[\bar{1}.377\bar{1}2.3770.359]_\alpha$, and $90^\circ/[1\bar{2}.38\bar{1}.380]_\alpha$ interviant boundaries, respectively (Fig. 4b).

The relative areas of all boundary planes as a function of orientation in the crystal reference frame, without considering the misorientation, are depicted in the standard stereographic projection for hexagonal crystals (Fig. 5). Here, the $(0001)_\alpha$ basal plane is

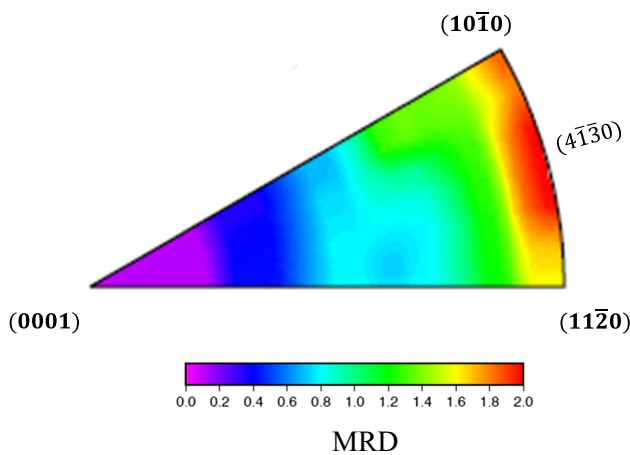


Figure 5 The distribution of grain boundary planes for all misorientations in the martensitic microstructure of Ti–6Al–4V alloy. MRD is the multiples of a random distribution.

placed in the centre of the stereogram and the prismatic planes (i.e. $\{11\bar{2}0\}_\alpha$ and $\{10\bar{1}0\}_\alpha$ planes) are within the circumference of the stereogram. The plot revealed an anisotropic distribution, having a maximum intensity of ~ 2.0 MRD. The relative areas of all orientation perpendicular to $[0001]_\alpha$ are high, and the peak is at the $\{4\bar{1}30\}_\alpha$ orientation (Fig. 5). It should be mentioned that the distribution minimum was positioned at the $(0001)_\alpha$ orientation (Fig. 5).

The boundary plane distributions at the specific misorientations associated with the interviant boundaries that arise from the Burgers OR are plotted in a stereographic projection in Fig. 6. The orientations of certain high symmetry grain boundary planes are also plotted for these misorientations, using Glowinski’s grain boundary toolbox software [60] (Fig. 6). Overall, the grain boundary plane distribution is anisotropic for all interviant boundaries. The $10.53^\circ/[0001]_\alpha$ interviant boundary plane distribution had no maxima higher than 0.5 MRD. Relative areas of this magnitude are deemed to be insignificant, so this distribution is not shown. The interviant boundary planes associated with the $60^\circ/[11\bar{2}0]_\alpha$ misorientation had a single maximum near the pyramidal $(\bar{1}101)_\alpha$ plane, indicating an ideal symmetric boundary with a maximum intensity of ~ 370 MRD (Fig. 6a). On the other hand, the boundary plane distribution of the $60.83^\circ/[\bar{1}.377\bar{1}2.3770.359]_\alpha$ interviant boundary had a maximum at the $(\bar{4}310)_\alpha$ orientation with an intensity of ~ 24 MRD, showing a near tilt character. (It

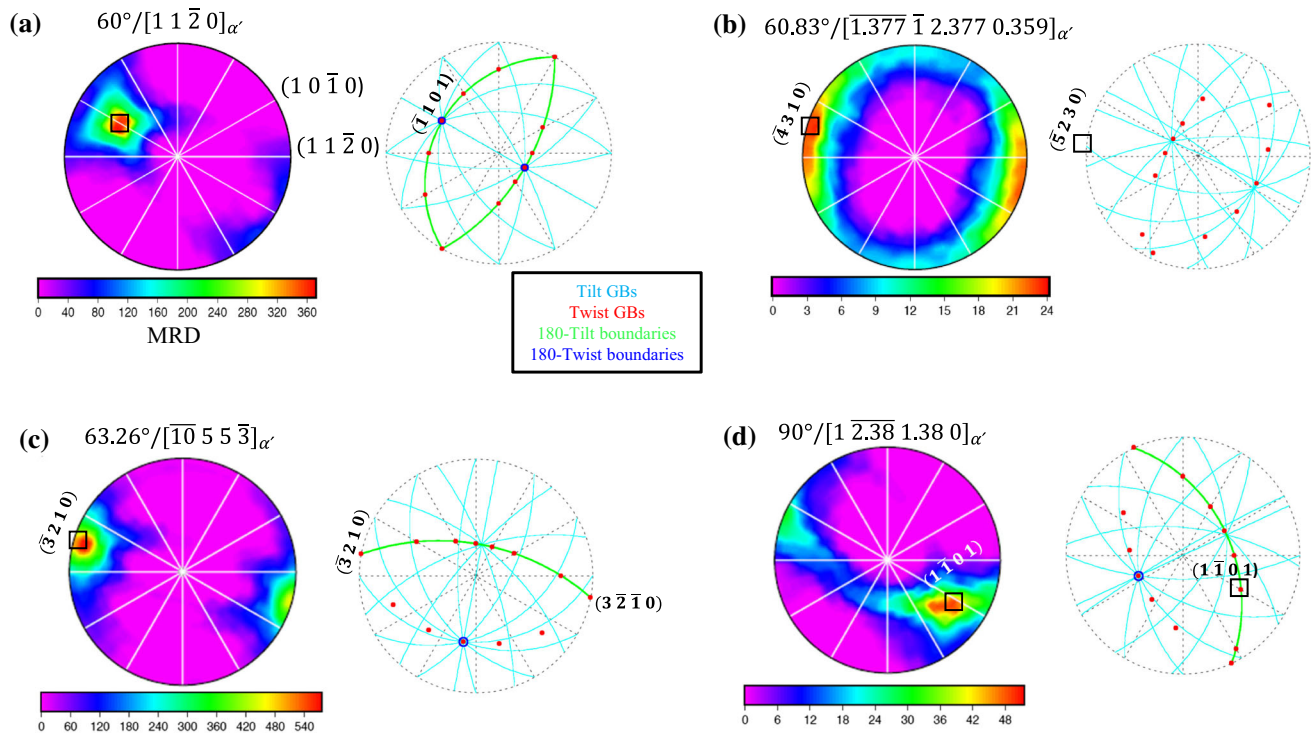


Figure 6 Distribution of intervariant interface/boundary planes character for different intervariants and the corresponding calculated geometrically characteristic boundaries in the martensitic microstructure.

deviates by $\sim 4^\circ$ from the ideal $(\bar{5}320)_{\alpha'}$ orientation, as shown in Fig. 6b.) The highly populated $63.26^\circ/[\bar{1}055\bar{3}]_{\alpha'}$ intervariant boundary had a strong peak (i.e. ~ 577 MRD) around the $(\bar{3}210)_{\alpha'}$ plane, displaying a twist character (Fig. 6c). The intervariant plane distribution for the $90^\circ/[\bar{1}2.38\bar{1}.380]_{\alpha'}$ had a diffuse maximum at the $(1\bar{1}01)_{\alpha'}$ plane with an intensity of ~ 52 MRD. This boundary plane orientation had a twist and 180° -tilt character, spreading between the $(1\bar{2}13)_{\alpha'}$ and $(\bar{4}3\bar{1}0)_{\alpha'}$ planes (Fig. 6d).

It is worth mentioning that the measurements of the five-parameter grain boundary plane distribution provided results that are qualitatively similar to those already reported in Reference [24]. The similarity of the current results (obtained with a spatial resolution of 10 nm) and the prior results (obtained with a spatial resolution of 150 nm) indicates that the grain boundary plane distribution is not sensitive to the spatial resolution of the orientation measurement within this range of resolutions.

Discussion

The grain boundary characteristic developed during the $\beta \rightarrow \alpha'$ transformation is largely related to martensite transformation mechanism and self-accommodation of the transformation strain. To explore the possible variant selection arrangements that alleviate accommodation of transformation strain, the crystallography of martensitic transformation is analysed for Ti-6Al-4V using the Burgers orientation relationship through elaborating the phenomenological theory of the martensitic transformation.

Variant selection and self-accommodation during $\beta \rightarrow \alpha'$ transformation

The martensitic transformation usually results in a relatively large shape change, which is accommodated by specific variant arrangement/s to minimize the associated strain energy. The grouping of martensite variants to minimize the transformation induced shear strain is known as the self-accommodation phenomenon [61], which influences microstructural characteristics including the texture and the intervariant boundary distribution. It appears

that the self-accommodation cluster in the Ti–6Al–4V martensitic microstructure has a V-shape and/or quadrilateral-variant assemblies (Fig. 2a).

Interestingly, the substructure of Ti–6Al–4V martensite laths reveals that the transformation is accommodated through twinning and/or dislocation slip (Figs. 2a, 3), which compensates the macroscopic shape change (lattice invariant deformation) that occurs during the martensitic transformation [62]. These characteristic features of the martensitic microstructure are significantly different from the martensitic laths observed in the CP–Ti alloy, where the martensitic transformation takes place only through slip [34]. Therefore, the phenomenological theory of the martensitic phase transformation is employed to analyse the shape deformation during the martensitic transformation in Ti–6Al–4V alloy.

In the phenomenological theory, the total deformation is a result of two invariant plane strains, one being the habit plane between two lattices and the other being the complementary strain, which is invisible on the macroscopic scale (Fig. 7). The complementary shear is required, as it is necessary to maintain the material integrity. In most martensitic transformations, the complementary shear is considered to be accommodated by a simple shear system (slipped martensite). Similar to slip, a twinning shear on a twinning plane can also produce an invariant plane. This results in two twin domains with specific thickness ratios, producing the shear strain for martensite transformation. In this regard, the Wechsler, Lieberman and Read’s (WLR) approach was employed to characterize the slipped and internally twinned cubic to orthorhombic martensitic transformation [53] and obtain a physically correct description of martensite transformation for the Ti–6Al–4V alloy.

The crystallography of martensite transformation in Ti–6Al–4V

The twins in Ti–6Al–4V martensite laths can produce invariant lattice shear (ILS). Therefore, the matrix after the lattice deformation should be transformed into twin domains with exact crystallographically equivalent correspondence having an appropriate thickness ratio, $(1 - x)/x$. In fact, the twinned region (i.e. denoted by domain 1 and 2 in Fig. 7c) formed from the parent phase is distorted by two crystallographically equivalent Bain distortions. In the WLR

approach, the two twin domains, firstly, need to maintain the exact crystallographically equivalent correspondence. Second, the prevalence of a plane in the parent β phase with a mirror symmetry is required. In other words, the shear plane must be a mirror plane of the parent crystal and the active twinning type determines which of the mirror planes [63, 64]. Considering the Bilby–Crocker criteria, the $\{110\}_\beta$ mirror planes can transform into the $\{10\bar{1}1\}_{\alpha'}$ planes (i.e. ILS twinning planes) [40, 65]. Therefore, the $(1\bar{1}01)_{\alpha'}/(101)_\beta$ twin systems for the BCC to HCP transformation are considered for the current calculation [66]. The Bain distortion matrices for the major and minor twin components of $(1\bar{1}01)_{\alpha'}$ and $(\bar{1}101)_{\alpha'}$ are described below as B_1 and B_2 , respectively.

$$B_1 = \begin{bmatrix} 1.07213 & 0.0431 & 0 \\ 0.0431 & 1.07213 & 0 \\ 0 & 0 & 0.9102 \end{bmatrix}$$

$$B_2 = \begin{bmatrix} 0.9102 & 0 & 0 \\ 0 & 1.07213 & -0.0431 \\ 0 & -0.0431 & 1.07213 \end{bmatrix} \tag{1}$$

The Bain distortion for the Ti–6Al–4V alloy is calculated by considering its lattice parameters ($a_\beta = 0.321$ nm, $a_{\alpha'} = 0.29216$ nm and $c_{\alpha'} = 0.46698$ nm) [67, 68]. The crystallographic correspondence is schematically presented in Fig. 7c. The total macroscopic shear (E) identifies a vector r in the parent BCC crystal, which is transformed into r' . This is resolved by considering two Bain distortions in the two twin-related regions and their corresponding rotations, which are given by the following equation.

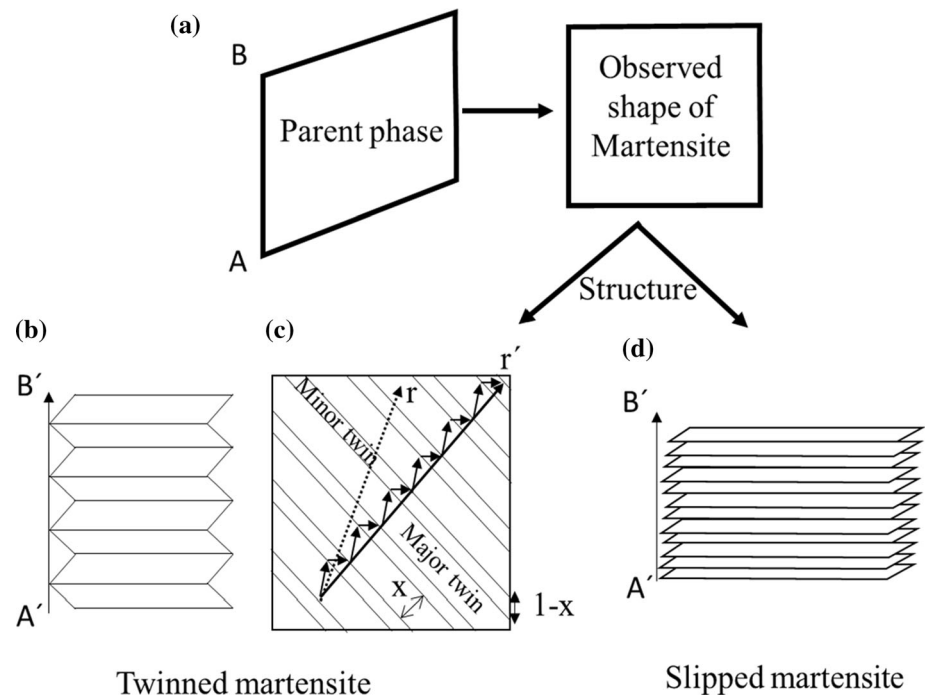
$$r' = \phi_1[(1 - x)B_1 + x\phi B_2]r = \phi_1 Fr \tag{2}$$

The rotation matrix, ϕ , for twinning on $(10\bar{1})_\beta$ corresponding to the variant plane of $(1\bar{1}01)_{\alpha'}$ is described by the Euler’s formula, as follows.

$$\frac{(p_1 - p_2)(q_1 - q_2)}{(p_1 - p_2)(q_1 + q_2)} = U \tan \frac{\theta}{2} \tag{3}$$

where p_1, q_1 and p_2, q_2 are the initial and final positions of the two vectors present in the undistorted plane, the U axis is the rotation axis, and θ is the angle of the rotation. Here, the rotation angle is 7.369° and ϕ is:

Figure 7 (a) Schematic illustration of the phenomenological theory of martensite. The heavy horizontal lines in (b) are coherent twin boundaries and (c) schematic diagram of an internally twinned martensite, the complementary twinning shear transforming original vector. (d) schematic of internally slipped martensite [40, 87].



$$\phi = \begin{bmatrix} 0.9917 & 0.0668 & -0.1092 \\ -0.0673 & 0.9977 & -0.0007 \\ 0.1089 & 0.0079 & 0.9939 \end{bmatrix} \quad (4)$$

Substituting the values of B_1 , B_2 and ϕ into Eq. (2) resolves F and the fraction of the symmetric and non-symmetric twin components (i.e. x). Thus, the distortion matrix, $E = \phi_1 F$, is calculated and summarized in Table 2 for the Ti-6Al-4V alloy. The predicted habit plane is $(\bar{0}.4037\bar{0}.5855\bar{0}.7028)_\beta$ which deviated only about 6.1° from the observed $\{344\}_\beta$ solution. Therefore, the predictions can be considered consistent for the further microstructure analysis [65, 69]. A detailed analysis of the Wechsler, Liberman and Read approach is presented in “Appendix”.

Considering the distortion matrix as the total strain imposed in the material for the nucleation of a given variant, the von Mises criterion for the martensite transformation of each variant (i.e. based on the dilatational (δ) and shear components (s) of the transformation) can be computed [34]. Accordingly, the lowest strain imposed by different groups of variant combinations (i.e. possible 132, 1320, and 11,880 for two-, three- and four-variant clustering, respectively) is calculated and summarized in Table 3.

Among different variant combinations, the four-variant configuration reveals the lowest equivalent

strains of 0.002782 and 0.002808 (Table 3). The intersection of variants in the four-variant combination gives rise to the intervariant boundaries with $63.26^\circ/[\bar{1}0\bar{5}5\bar{3}]_{\alpha'}$ and $60^\circ/[1\bar{1}\bar{2}0]_{\alpha'}$ and $90^\circ/[1\bar{2}.38\bar{1}.380]_{\alpha'}$ misorientations (Table 1). This suggests that the four-variant ($V_1V_2V_4V_5$) morphological clustering might promote these intervariant boundaries. The most probable configuration, therefore, consists of two pairs with a V-shape morphology (i.e. four-variant clustering), each consisting of two distinct variants, as shown schematically in Fig. 8c. This morphological clustering can explain the current observation of V-shape and quadrilateral arrangements in the microstructure. The crystallographic four-variant arrangement leads to the promotion of three distinct intervariant boundaries, namely $63.26^\circ/[\bar{1}0\bar{5}5\bar{3}]_{\alpha'}$, $60^\circ/[1\bar{1}\bar{2}0]_{\alpha'}$ and $90^\circ/[1\bar{2}.38\bar{1}.380]_{\alpha'}$, where $63.26^\circ/[\bar{1}0\bar{5}5\bar{3}]_{\alpha'}$ and $90^\circ/[1\bar{2}.38\bar{1}.380]_{\alpha'}$ have the highest and lowest fraction, respectively (Fig. 8). This is consistent with the observed intervariant boundary fractions for the martensitic Ti-6Al-4V alloy, where the highest fraction is related to $63.26^\circ/[\bar{1}0\bar{5}5\bar{3}]_{\alpha'}$ followed by $60^\circ/[1\bar{1}\bar{2}0]_{\alpha'}$ and a smaller population of $90^\circ/[1\bar{2}.38\bar{1}.380]_{\alpha'}$ boundaries (Fig. 4b). It is worth mentioning that $60^\circ/[1\bar{1}\bar{2}0]_{\alpha'}$ boundaries are also promoted through the transformation twin within the

Table 2 The typical calculated crystallographic sets considering the activation of $\{101\}_\beta <10\bar{1}\rangle_\beta$ twin system

Twin system	Habit plane (P_β)	Rotation matrix	E (distortion matrix)
$\{101\}_\beta <10\bar{1}\rangle_\beta$	$\begin{pmatrix} 0.4037 \\ 0.5855 \\ 0.7028 \end{pmatrix}$	$\begin{bmatrix} 0.998 & -0.0619 & 0.0126 \\ 0.0619 & 0.9979 & -0.0072 \\ -0.012 & 0.0072 & 0.9998 \end{bmatrix}$	$\begin{bmatrix} 0.9619 & -0.0801 & 0.1171 \\ 0.0967 & 1.06866 & -0.0001 \\ -0.1007 & -0.0407 & 0.9976 \end{bmatrix}$

Table 3 The von Mises equivalent strain calculated for different combinations of variant cluster arrangements in the martensitic transformation

Twin system	Two-variant	Three-variant	Four-variant
$\{101\}_\beta <10\bar{1}\rangle_\beta$	Min ϵ_{ave} 0.0067 V_1V_7 V_2V_{11} V_3V_6	Min ϵ_{ave} 0.0083	$V_1V_7V_{10}$ $V_8V_4V_2$ Min ϵ_{ave} 0.002782 and 0.002808 $V_1V_2V_4V_5V_3V_4V_{11}V_{12}$ $V_5V_6V_8V_9$ $V_1V_2V_4V_5$ and $V_1V_4V_5V_8$

martensitic laths (Fig. 2a), which is the mechanism of martensitic transformation in Ti–6Al–4V alloy.

Interestingly, the morphological arrangements and the intervariant boundary population for the martensitic Ti–6Al–4V alloy are significantly different from the previous observation of martensitic CP–Ti [34]. It was observed that the transformation strain is accommodated by slipped martensitic laths in the commercially pure titanium compared to the twinning for the Ti–6Al–4V. This change in the martensite transformation mechanism is a result of a significantly different shape strain, leading to three-variant clustering and an increase in the population of $60^\circ/[11\bar{2}0]_\alpha$ intervariant boundaries (i.e. 60% of total boundary population) [34]. Therefore, the current result shows that the change in the chemical composition of the Ti alloy results in different Bain deformation (i.e. by changing the lattice parameters) during the martensite transformation. This consequently alters the martensite transformation mechanism (i.e. slip vs twinning), promoting different variant cluster arrangement/s, and ultimately specific intervariant boundaries. In addition, the presence of other intervariant boundaries is, most likely, due to the intersection of different four-variant clusters.

It is worth mentioning that the overall texture can also influence the grain boundary populations. Here, the overall texture of martensite is dictated by the prior beta texture. However, all possible 12 variants are formed during the martensitic transformation in a given prior beta grain. Therefore, the grain boundary network in the martensitic microstructure is largely

governed by the local variant selection mechanism. In other words, the effect of prior beta texture is limited to the boundaries formed due to the intersection of variants on either side of prior beta boundaries, which do not have any specific crystallographic relationship. These boundaries form a small fraction of the grain boundary population (Fig. 4a), resulting in a negligible influence on the overall grain boundary network.

Characteristics of martensitic intervariant interfaces

The intervariant boundaries associated with the martensitic Ti–6Al–4V alloy had a peak intensity at a specific boundary plane orientation. The highly populated $63.26^\circ/[\bar{1}055\bar{3}]_\alpha$ intervariant boundary was associated with the $(\bar{3}210)_\alpha$ boundary plane orientation, showing a twist and properly quasi-symmetric character (Fig. 6c) [70]. This means that the crystallographic planes on both sides of the $63.26^\circ/[\bar{1}055\bar{3}]_\alpha$ intervariant boundary had equivalent Miller indices. This tendency for specific intervariant boundary plane is significantly different from the previous results on martensitic CP–Ti [34]. The dominant intervariant boundary for the martensitic CP–Ti has the $60^\circ/[11\bar{2}0]_\alpha$ misorientation with the $(\bar{1}101)_\alpha$ boundary plane with a symmetric tilt and improper quasi-symmetric tilt character. In polycrystalline alloys subjected to a given processing route, it is expected that the change in the chemical composition provides similar grain boundary plane

Table 4 The interplanar spacing (d_{hkl}) for different measured intervariant planes and their corresponding population

Intervariant boundary		Intensity (MRD)	Interplanar spacing (Å)
Axis/angle	Plane		
Figure 5			
All boundaries	$(10\bar{1}0)_{\alpha'}$	1.9	0.8519 or 1.7038*
	$(11\bar{2}0)_{\alpha'}$	1.65	1.4755
	$(0001)_{\alpha'}$	0	2.0283
	$(10\bar{1}1)_{\alpha'}$	1	0.3604 or 1.8019*
	$(4\bar{1}\bar{3}0)_{\alpha'}$	2.01	0.2363 or 0.4725*
Figure 6			
$10.53^\circ/[0001]_{\alpha'}$	$(19\bar{8}\bar{1}\bar{1}0)_{\alpha'}$	0.4	0.1547
$60^\circ/[11\bar{2}0]_{\alpha'}$	$(\bar{1}101)_{\alpha'}$	370.7	0.3604 or 1.8019*
$60.83^\circ/[\bar{1}.377\bar{1}2.3770.359]_{\alpha'}$	$(\bar{4}310)_{\alpha'}$	24.15	0.3219
	$(\bar{5}320)_{\alpha'}$	21.00	0.1954 or 0.3908*
$63.26^\circ/[\bar{1}055\bar{3}]_{\alpha'}$	$(\bar{3}210)_{\alpha'}$	490	0.3219 or 0.6439*
$90^\circ/[1.2381.380]_{\alpha'}$	$(1\bar{1}01)_{\alpha'}$	51.58	0.0416 or 0.0833*

*Taking into account the structure factor as the plane passing through an additional atom [82]

orientations for a specific boundary, though the population may differ [71–73]. In particular, the grain boundary population for the $\Sigma 3$ annealing twin boundaries increases with a decrease in the stacking fault energy (SFE) of the materials having face-centred cubic structure [26]. For the current study, the change in the chemical composition of Ti alloy affects the martensitic phase transformation mechanism from the dislocation slip in CP–Ti to the twin assisted in Ti–6Al–4V alloy. This change in the martensite transformation mechanism influences the self-accommodation of martensite shape strain and ultimately leads to a distinct variant arrangement from three-variant cluster in the CP–Ti [34] to V-shape and/or quadrilateral clusters in the Ti–6Al–4V alloy. Therefore, the intervariant boundary population for the examined martensitic Ti–6Al–4V alloy (Fig. 4b) is significantly different from the one reported for the martensitic CP–Ti microstructure [34]. Moreover, it can be implied that the change in the chemical composition can affect the dominant intervariant boundary plane in the martensitic Ti alloy microstructure through altering the phase transformation mechanism.

Although past studies of grain boundary characteristics in Ti alloys are limited, it is well established that grain boundary populations have an inverse relationship with the related boundary energy for cases where the microstructures form by grain growth [24, 56, 74–79]. Using the interplanar spacing

as the criteria to analyse the grain boundary energy [80–82], it was observed that the low energy interfaces in martensitic CP–Ti alloys are associated with the lowest population [34]. A similar observation can be also observed in the martensitic Ti–6Al–4V alloy where the low energy interfaces (i.e. the basal $(0001)_{\alpha'}$ plane with interplanar spacing of 2.0283 Å, Table 4) constitute the lowest population. In parallel, the interplanar spacings of the observed characteristic planes have also been computed and summarized in Table 4. Four-variant clustering largely leads to the promotion $63.26^\circ/[\bar{1}055\bar{3}]_{\alpha'}$ and $60^\circ/[11\bar{2}0]_{\alpha'}$, having a population of $\sim 38\%$ and $\sim 33\%$, respectively (Fig. 4b). The latter mostly terminated on the pyramidal $(\bar{1}101)_{\alpha'}$ plane and have a maximum intensity of ~ 370 MRD (Fig. 6a). This boundary is also both proper and improper quasi-symmetric (Fig. 6a), as the $[11\bar{2}0]_{\alpha'}$ axis is a twofold symmetry axis [70]. The $(\bar{1}101)_{\alpha'}$ plane has the second largest interplanar spacing (i.e. 1.8019 Å, Table 4), suggesting a relatively low energy configuration. This is consistent with the molecular dynamics energy calculation [83], showing that the pyramidal $(\bar{1}101)_{\alpha'}$ plane has the minimum energy (168.7 mJ/m²) among the $[11\bar{2}0]_{\alpha'}$ tilt boundaries. It is worth mentioning that among other sets of planes predicted to have low energies by the molecular dynamic calculation, such as $(\bar{1}013)_{\alpha'}$, $(\bar{1}012)_{\alpha'}$ and $(\bar{2}021)_{\alpha'}$, at rotation angles of 31.39°, 42.47° and 74.7°, respectively, only the 31.39° was

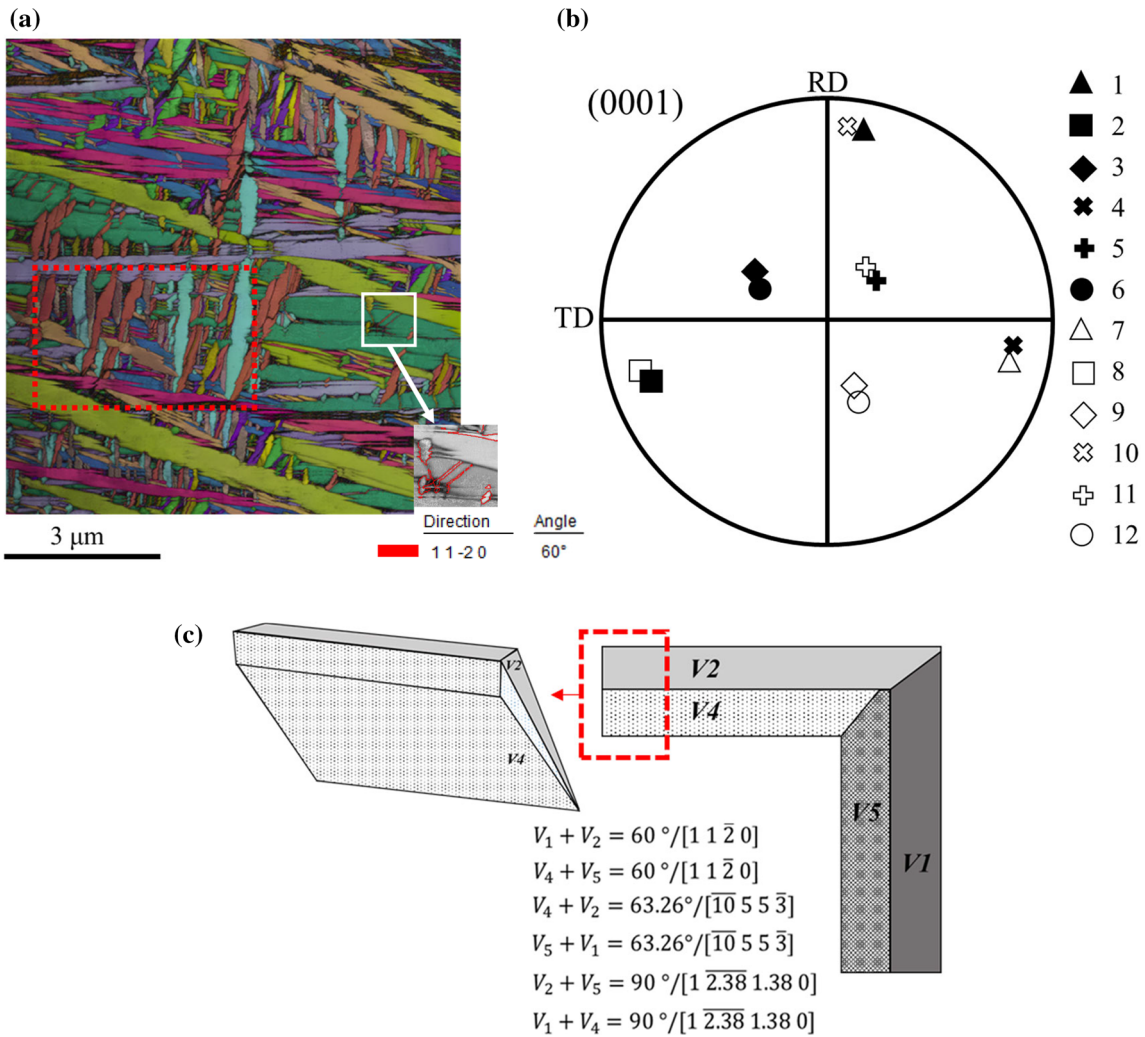


Figure 8 (a) Inverse pole figure map of the martensitic microstructure in the Ti-6Al-4V alloy, (b) the corresponding variants' (0001)_α poles and (c) schematic illustration of the martensitic lath clustering.

present in the misorientation angle distribution of the martensite sample. This suggests that the martensitic transformation in Ti-6Al-4V alloy and the associated crystallographic constraints can simultaneously provide low energy configurations in the form of four-variant clustering and terminate on pyramidal planes. However, it is not always the case, as the $63.26^\circ / [\bar{1}\ 0\ 5\ 5\ \bar{3}]_{\alpha'}$ intervariant boundaries having the highest population terminate near to the $(\bar{3}\ 2\ 1\ 0)_{\alpha'}$ tilt boundary (Fig. 6c), with a relatively high energy boundary plane configuration (Table 4).

Connectivity of the grain boundary network

The intervariant boundary network characteristics (i.e. connectivity of the intervariants) were measured through the analysis of triple junctions in the martensitic microstructure of Ti-6Al-4V alloy. As observed in Fig. 4b, the total length fraction of intervariant boundaries contained above 99% of the total boundary fraction. Therefore, the triple junction analysis based on the intervariant boundaries can represent a clear view of the boundary connectivity and network throughout the microstructure. To this end, the boundaries, which deviated from the ideal intervariant lattice misorientations by 5° or more, were initially eliminated from the microstructure.

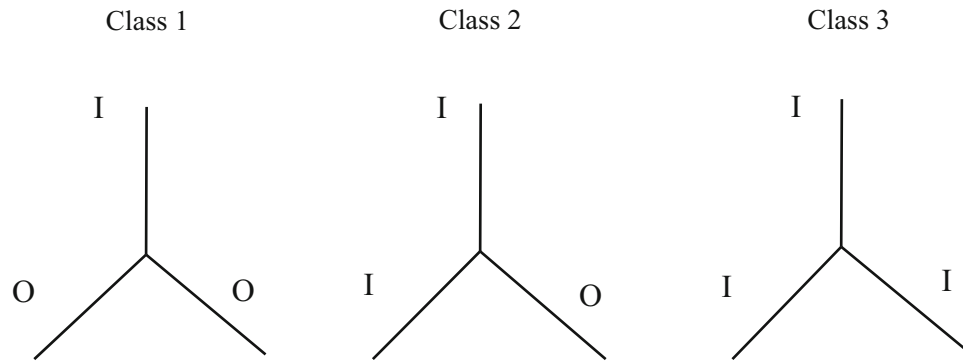


Figure 9 Classification of triple junctions based on the intervariant boundary type associated with Burgers orientation relationship. *I* and *O* represent the intervariant boundary of interest and the other intervariant boundaries. For example, if the boundary of interest, *I*, is

$60^\circ/[1\ 1\ \bar{2}0]_{\alpha'}$, other intervariant boundaries, *O*, would be one of the remaining intervariant boundaries associated with Burgers OR (i.e. $10.53^\circ/[0\ 0\ 0\ 1]_{\alpha'}$, $60.83^\circ/[\bar{1}.377\ \bar{1}\ 2.377\ 0.359]_{\alpha'}$, $63.26^\circ/[\bar{1}0\ 5\ 5\ \bar{3}]_{\alpha'}$ and $90^\circ/[1\ \bar{2}.38\ 1.38\ 0]_{\alpha'}$).

Then, the triple junctions were identified in the martensitic microstructure of Ti–6Al–4V alloy using an in-house software. The triple junctions were classified based on the presence of specific intervariant boundary type. In other words, the collected triple junctions were categorized into three different classes, from 1 through 3, representing the number of a specific intervariant boundary type at the triple junction. For example, the class 2 triple junction means that it consists of two similar intervariant boundaries and one boundary related to other intervariant boundary types (Fig. 9). Similar analysis was carried out on the martensitic CP–Ti microstructure in reference [34] to investigate the effect of local variant selection as a result of distinct martensitic mechanism on the grain boundary network.

Figure 10 displays the number fraction of different classes of triple junctions for all five types of intervariant boundaries in the CP–Ti and Ti–6Al–4V martensitic microstructures. In total, 35,530 and 21,447 triple junctions were analysed in the CP–Ti and Ti–6Al–4V martensitic microstructures, respectively. The triple junction distribution for the martensitic Ti–6Al–4V alloy is significantly different from the martensitic CP–Ti (Fig. 10a, b). For the latter, the number fraction of triple junctions consisting of three $60^\circ/[1\ 1\ \bar{2}0]_{\alpha'}$ intervariant boundaries (i.e. class 3) is significantly higher (53%) compared to the other triple junction classes, and only $\sim 1\%$ of the triple junctions belong to class 2. (Only two $60^\circ/[1\ 1\ \bar{2}0]_{\alpha'}$ intervariants meet at the triple junction, as shown in Fig. 10a.) For the Ti–6Al–4V martensitic

microstructure, the number fraction of the class 3 triple junction for the $60^\circ/[1\ 1\ \bar{2}0]_{\alpha'}$ is significantly lower ($\sim 15\%$). By contrast, the class 3 triple junctions for the $63.26^\circ/[\bar{1}0\ 5\ 5\ \bar{3}]_{\alpha'}$ are $\sim 10\%$ of the total number of triple junctions, which is much higher than for the CP–Ti martensitic microstructure ($\sim 2\%$, Fig. 10b). The other intervariant boundary types largely belong to the class 1 triple junction categories for both martensitic microstructures (Fig. 10a, b).

The average boundary length for a given intervariant boundary between two triple junctions in the martensitic CP–Ti and Ti–6Al–4V alloy was also measured (Fig. 10c, d). In general, the average length of intervariant boundaries in the martensitic CP–Ti is much greater than the ones measured in the Ti–6Al–4V martensite. This is not surprising as the latter reveals a much finer microstructure than the CP–Ti martensite (Fig. 10c, d). However, the average boundary length for the Type 1, Type 3 and Type 5 intervariant boundaries is similar for both martensitic microstructures (Fig. 10c, d). The highest average boundary length is associated with the Type 2 and Type 4 intervariant boundaries for the martensitic CP–Ti, having the values of ~ 4.81 and $\sim 4.31\ \mu\text{m}$, respectively (Fig. 10c). However, these values are much different for the martensitic Ti–6Al–4V alloy where the highest average length belongs to the Type 4 intervariant boundary ($\sim 0.18\ \mu\text{m}$), and the Type 2 intervariant has the second highest length ($\sim 0.15\ \mu\text{m}$). For the martensite CP–Ti, the promotion of the $60^\circ/[1\ 1\ \bar{2}0]_{\alpha'}$ intervariant boundary population through the formation of a triangular

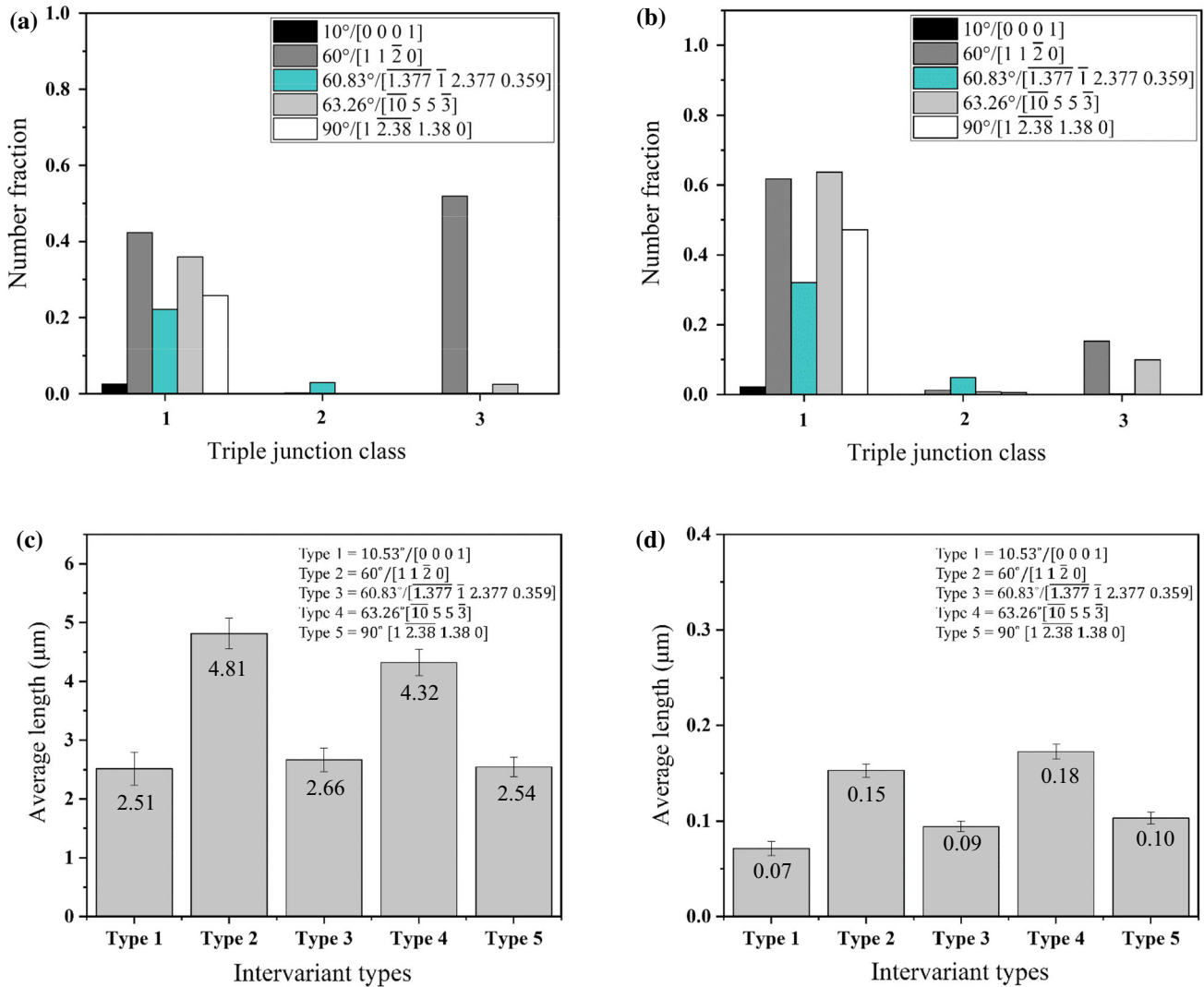


Figure 10 Fraction of specific types of intervariant boundaries present in different types of triple junctions for (a) CP-Ti and (b) Ti-6Al-4V, and the average length of the intervariant boundaries between the triple junctions in the microstructure for

the martensitic (c) CP-Ti and (d) Ti-6Al-4V. Triple junction class 1 denotes the presence of at least on intervariant boundary of interest and class 3 indicates that all the boundaries in the triple junction are of the intervariant boundary of interest.

morphology results in an increase in the length of $60^\circ/[11\bar{2}0]_{\alpha'}$ compared to the other intervariant boundaries. On the contrary, an increased population of the $63.26^\circ/[\bar{1}055\bar{3}]_{\alpha'}$ boundary in the martensite Ti-6Al-4V alloy through the formation of quadrilateral-variant clustering slightly enhances the average length of this intervariant boundary compared to the $60^\circ/[11\bar{2}0]_{\alpha'}$ intervariant (Fig. 4). Therefore, the changes in the variant arrangements of martensitic Ti alloys can also result in different average lengths for the intervariant boundaries.

The boundary triple junction analysis reveals a significant change in the grain boundary network

due to the difference in the martensitic transformation mechanism in Ti alloys (Fig. 10). In the martensite CP-Ti, the shear martensitic transformation appears to enhance the connectivity of the $60^\circ/[11\bar{2}0]_{\alpha'}$ intervariant boundaries at the triple junctions (~ 50% of class 3 triple junction) due to the three-variant clustering, significantly promoting the $60^\circ/[11\bar{2}0]_{\alpha'}$ boundary (refer to reference [34]). However, the class 3 triple junction frequency is significantly reduced for the $60^\circ/[11\bar{2}0]_{\alpha'}$ boundary in the martensitic Ti-6Al-4V microstructure (to ~ 15%), while the $63.26^\circ/[\bar{1}055\bar{3}]_{\alpha'}$ class 3 triple junction increases to ~ 10%. This is consistent with the

morphological features observed in the martensitic Ti–6Al–4V microstructure, where the quadrilateral-variant clustering is dominant due to the twin-assisted martensitic transformation mechanism, promoting the formation of $63.26^\circ/[\bar{1}0\bar{5}5\bar{3}]_{\alpha'}$ and $60^\circ/[11\bar{2}0]_{\alpha'}$ intervariant boundaries (Figs. 4 and 8). This suggests that the change in the Ti alloy chemical composition can significantly alter the network of the boundaries within the microstructure through varying the martensitic phase transformation mechanism. This finding can be employed as a novel approach to engineer the grain boundary network in Ti alloys for a property of interest through the phase transformation.

Conclusion

In the current study, the intervariant boundary network characteristics of a Ti–6Al–4V alloy subjected to a martensitic phase transformation were investigated through the crystallographic theories of displacive transformations, five-parameter grain boundary analysis and triple junction analysis. The followings are the most important findings:

- (1) Twinned martensitic laths were observed for the $\beta \rightarrow \alpha'$ transformation in Ti–6Al–4V alloy. The crystallography associated with the transformation was investigated by the WLR theory and compared with the experimental measurements. The important elements associated with the theoretical calculation of the crystallographic features were the inhomogeneity and distortion that led to the formation of twinned α' laths. The calculated habit plane was relatively close to the experimentally measured habit plane (i.e. 6.1° deviation).
- (2) The phenomenological theory of martensite revealed that the strain energy of the transformation is accommodated through the formation of four specifically oriented variants. This prediction was consistent with the frequently detected morphological features in the martensite microstructure, where a quadrilateral morphology (four-variant clustering) consisted of two V-shape intersecting laths with complementary orientations was observed. This

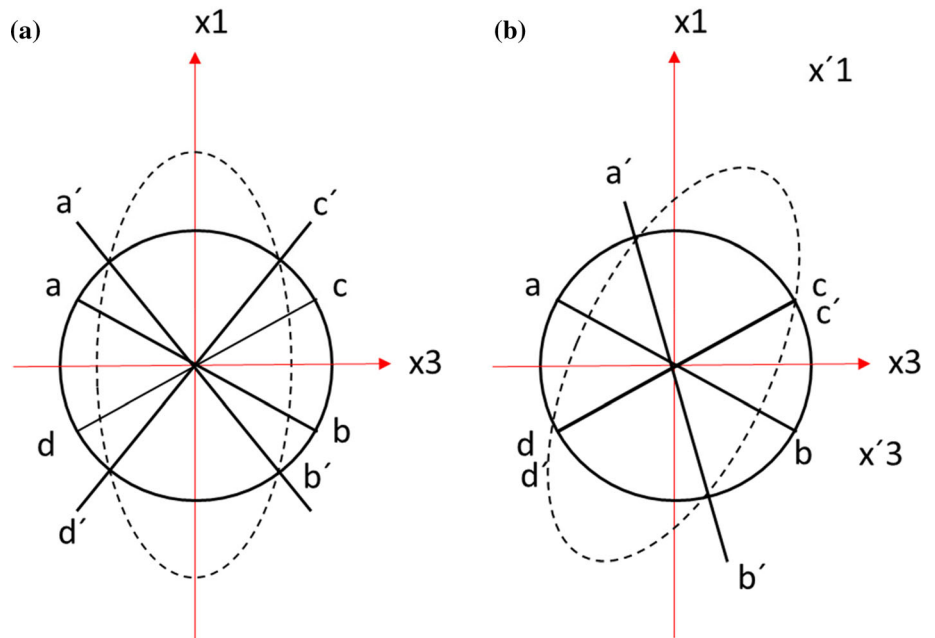
specific crystallographic arrangement promoted $63.26^\circ/[\bar{1}0\bar{5}5\bar{3}]_{\alpha'}$ and $60^\circ/[11\bar{2}0]_{\alpha'}$ intervariant boundaries, accounting for $\sim 38\%$ and 33% of the total boundary population, respectively.

- (3) The five-parameter analysis of the intervariant boundaries revealed the tilt/twist/mixed character of the intervariant boundaries. The intervariants associated with the four-variant clusters naming the $63.26^\circ/[\bar{1}0\bar{5}5\bar{3}]_{\alpha'}$ and $60^\circ/[11\bar{2}0]_{\alpha'}$ intervariants had a twist $(\bar{3}210)_{\alpha'}$ plane and symmetric tilt $(10\bar{1}1)_{\alpha'}$ character, respectively. The comparison of the results with previous studies showed that the change in the chemical composition of Ti alloys may not lead to a change in α'/α' intervariant boundary characteristics.
- (4) The distribution of triple junctions in martensitic Ti–6Al–4V alloy was characterized based on the intersecting intervariant boundary and then compared with CP–Ti martensite. The distribution for Ti–6Al–4V was significantly different from the distribution in CP–Ti. The most connected intervariant boundary at the triple junctions appeared to be $60^\circ/[11\bar{2}0]_{\alpha'}$ in the CP–Ti martensite microstructure, whereas the connectivity of $63.26^\circ/[\bar{1}0\bar{5}5\bar{3}]_{\alpha'}$ intervariant boundary in the Ti–6Al–4V martensite was greater than the $60^\circ/[11\bar{2}0]_{\alpha'}$ intervariant boundary. This difference showed that the change in the martensitic transformation mechanism (slip vs twinning) associated with the chemical composition may significantly affect the grain boundary network in Ti alloys. This may indicate that the theory of martensite can be successfully used to predict the grain boundary network of martensitic microstructures in Ti alloys.

Acknowledgements

Extensive discussions with Prof. Bevis Hutchinson are greatly acknowledged. Deakin University's Advanced Characterization Facility is acknowledged for use of the EBSD instruments and assistance from Dr. Mark Nave. Financial support provided by the

Figure 11 (a) The effect of Bain strain (dashed ellipsoid) on the parent phase (solid circle), (b) after combination with a rigid body rotation. The invariant line “cd” can be observed in (b) [40, 87].



Australian Research Council is gratefully acknowledged.

Appendix

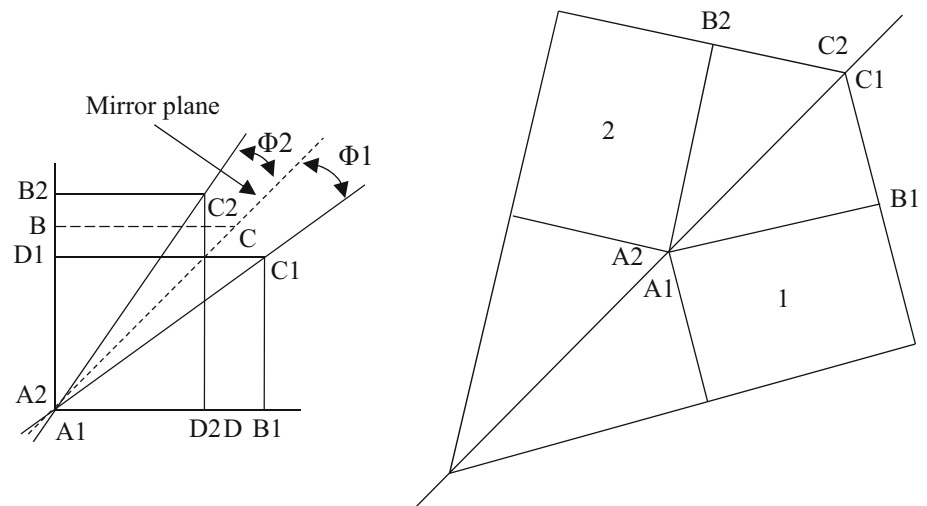
Phenomenological theory of martensite transformation

The phenomenological theory of martensite transformation, which is based on the double shear mechanism introduced by Greninger-Troiano [84], has been developed by Bowles and Mackenzie (B–M theory [85, 86]) and by Wechsler, Lieberman, and Read (W–L–R theory [52, 53]). This implies that the crystallographic changes during the martensite transformation produce a linear strain resulting in existence of an interface plane with no rotation and distortion (invariant plane) at the vicinity of the martensite lath and the matrix. Thus, the strain (i.e. deformation) on this plane is called invariant plane strain. However, for an employed homogeneous deformation resulting from the crystallographic changes of the parent and product lattices, known as the Bain deformation, an invariant plane condition cannot be met. This can be generally observed through the imposing of the Bain distortion on sphere parent crystal. The deformation resulting in an

ellipsoid shape shows that no lines or planes in the parent sphere crystal (shown by letters in Fig. 11a) can be unextended or undistorted, meaning that the Bain distortion is not an invariant plane strain in nature. In this regard, there should be an additional shear, which does not impose a macroscopic shape, although having a microscopically inhomogeneous character. This lattice invariant shear (LIS), when superimposed on the Bain strain, results in an invariant plane within the shear transformation. Since the LIS cannot produce any crystal changes, it should have an inhomogeneous character such as deformation by dislocation slip or twinning. This can be illustrated in Fig. 7 where the lattice strain changes the initial crystal into a deformed one (Fig. 7a), and thus, the magnitude of $A'B'$ vector can be brought back to AB through a lattice invariant shear either by slip (Fig. 7d) or twinning (Fig. 7c) [40, 87]. Moreover, there should be an additional rotation within the matrix to coincide the $A'B'$ vector with the original AB (Fig. 7b).

Therefore, the martensite transformation should consist of a lattice deformation (Bain distortion), a lattice invariant shear and a lattice rotation, which can be represented in a matrix form of B , P and R , respectively. The total shape deformation can be represented, as $P_1 = RBP$. P_1 can be described by assuming the lattice invariant shear P . Based on the prior descriptions and the fact that the LIS can be ascertained by slip or twinning, the total shape

Figure 12 Schematic representation of the symmetry correspondence between two crystallographic variants [40].



deformation in martensite transformation is described through Wechsler, Lieberman and Read theories in the following.

Wechsler–Lieberman–Read theory

Here, the shape deformation is presented as the P_1 , which can be described through the production of three matrices as follows:

$$P_1 = RBP \tag{5}$$

where the R , B and P are known as the rigid body rotation, lattice deformation and a simple shear, respectively. It is now necessary to determine the plane and direction for the lattice invariant shear. The rigid body rotation does not change the length of any vectors; therefore, the vector v must remain unchanged in magnitude as a result of the combination of P and B . Meaning,

$$v'P'B'BPz = v'v \tag{6}$$

Here, the prime mark denotes the transpose of the matrix. Through this equation, the habit plane is determined as an undistorted plane.

If the combination matrix of BP can be defined as F , the relation changes into:

$$v'F'Fv = v'v \tag{7}$$

Now, it is more convenient to express F as the product of an orthogonal matrix R_3 and a symmetric matrix F_s . Therefore, the F_s can be diagonalized by means of orthogonal transformation:

$$z' = R_4z \tag{8}$$

In this regard, in the basis where the F_s is diagonal, the P_1 can be described as:

$$P_1 = RR_3R_4F_dR_4' \tag{9}$$

where F_d is a diagonal matrix described as:

$$F_d = \begin{bmatrix} \lambda_1 & 0 & 0 \\ 0 & \lambda_2 & 0 \\ 0 & 0 & \lambda_3 \end{bmatrix} \tag{10}$$

Now, based on the this theorem, where the condition for Eq. (6) is the presence of an undistorted plane, one of the eigenvalues of F_d must remain unity and the eigenvector must remain in the undistorted plane, which gives,

$$F'F = R_4F_d^2R_4' \tag{11}$$

Therefore, a characteristic equation:

$$\text{Det}(F'F - \lambda^2I) = 0 \tag{12}$$

which can be solved. Here, I is the identity matrix.

Now, an orthonormal basis, which the lattice invariant shear takes from, needs to be introduced. This basis is defined by R_5 as a 3 by 3 matrix, where each column defines the unit shear direction (i.e. slip direction, d_2), the unit vector parallel to the shear plane normal (i.e. slip plane normal, p_2) and t through the cross product of d_2 and P_2 .

In this regard, the P in the orthonormal basis (P_0) can be defined as:

$$P_o = \begin{bmatrix} 1 & g & 0 \\ 0 & 1 & 0 \\ 0 & 0 & 1 \end{bmatrix} \tag{13}$$

Now, Bain strain can be transformed into the orthonormal basis through,

$$B_o = R'_5 B R_5 \tag{14}$$

Then, F can be defined easily in the orthonormal basis,

$$F_o = B_o P_o \tag{15}$$

In this regard, Eq. (12) takes a quadratic form and can be solved. Concurrently, the corresponding eigenvectors define the orthogonal matrix R_4 , which as indicated diagonalizes the $F'F$ (i.e. Eq. 11).

Now, the g value and the undistorted plane in Eqs. 6 and 13 can be solved, respectively. The R can be also obtained using the Euler theorem. Here, two vectors in the habit plane can be considered in the orthonormal basis, naming σ and ϑ . Then, the vectors should be defined in the orthogonal matrix R_4 , as $\bar{\sigma}$ and $\bar{\vartheta}$. The magnitude of u (i.e. vector parallel to the desired axis of rotation) and the tangent half angle of the rotation can be obtained:

$$\frac{[\bar{\vartheta} - \vartheta] \times [\bar{\sigma} - \sigma]}{[\bar{\sigma} - \sigma] \cdot [\bar{\vartheta} + \vartheta]} = u \tan\left(\frac{\theta}{2}\right) \tag{16}$$

Then, u and θ can be utilized to calculate the rigid body rotation (R). The R and P_1 values can be obtained using the following equation and Eq. 6, respectively:

$$R = \begin{bmatrix} \alpha_{11}^2 \beta + \cos \theta & \alpha_{11} \alpha_{12} \beta - \alpha_{31} \sin \theta & \alpha_{11} \alpha_{31} \beta + \alpha_{21} \sin \theta \\ \alpha_{21} \alpha_{11} \beta + \alpha_{31} \sin \theta & \alpha_{21}^2 \beta + \cos \theta & \alpha_{21} \alpha_{31} \beta - \alpha_{11} \sin \theta \\ \alpha_{31} \alpha_{11} \beta + \alpha_{21} \sin \theta & \alpha_{31} \alpha_{21} \beta + \alpha_{11} \sin \theta & \alpha_{31}^2 \beta + \cos \theta \end{bmatrix} \tag{17}$$

where the α_{ij} are the indices for the orthonormal matrix R_5 .

For the accommodation of lattice invariant strain through twinning, the parent phase is evolved through two twin-related orientations in the martensitic phase. Therefore, two equivalent crystallographic strains need to be operated to produce two twin-related variants in the product phase. This is expected to form the symmetry configuration point of view, as the transformation process has a general tendency to restore the reduction in symmetry elements through creating a number of crystallographic variants. An illustration of such is depicted in Fig

12. It is observed that the parent lattice indicated by the notation ABCD produces two twin-related equivalent lattices. Therefore, the parent lattice loss of mirror symmetry is compensated through forming the twinned product crystals.

For such transformation, the lattice deformation (Bain strain, B_1) for the two twin-related orientations can be represented in their principal axes systems, as follows:

$$B'_1 = \begin{bmatrix} \eta_1 & 0 & 0 \\ 0 & \eta_2 & 0 \\ 0 & 0 & \eta_3 \end{bmatrix} \tag{18}$$

$$B'_2 = \begin{bmatrix} \eta_1 & 0 & 0 \\ 0 & \eta_3 & 0 \\ 0 & 0 & \eta_2 \end{bmatrix}$$

However, it is more convenient to represent the lattice strains in the parent crystal coordinate system, meaning that the axis system of the martensite crystals should be rotated into the parent phase. Therefore, B_1 and B_2 can be obtained, as follows:

$$B_1 = \begin{bmatrix} \frac{\eta_1 + \eta_2}{2} & \frac{\eta_2 - \eta_1}{2} & 0 \\ \frac{\eta_2 - \eta_1}{2} & \frac{\eta_1 + \eta_2}{2} & 0 \\ 0 & 0 & \eta_3 \end{bmatrix} \tag{19}$$

$$B_2 = \begin{bmatrix} \frac{\eta_1 + \eta_2}{2} & 0 & \frac{\eta_2 - \eta_1}{2} \\ 0 & \eta_3 & 0 \\ \frac{\eta_2 - \eta_1}{2} & 0 & \frac{\eta_1 + \eta_2}{2} \end{bmatrix}$$

Similar to the Bowles and Mackenzie theory, B_1 and B_2 can be brought into twin-related orientations through a rigid body rotation of ϕ_1 and ϕ_2 , respectively. These rotations are indicated by the 1 and 2 numbers, respectively, as clearly observed in Fig. 12. Therefore, ϕ_1 and ϕ_2 describe the rotations of the principal axes of the pure distortions in regions 1 and 2 relative to an axis system fixed in the untransformed parent phase.

It should be considered that the volume fraction of each orientation can be expressed in terms of their thickness ratio, which is determined based on the IPS condition required for the lattice invariant deformation. Therefore, an arbitrary vector such as r in the matrix (Fig. 7) becomes like a twinned martensite crystal shown as a zigzag line where each orientation consumes a thickness of $(1 - x)$ and x , respectively.

The transformation of vector r into the r' can be expressed as the sum of the vectors $OV = OA + AB + BC + \dots + UV$ or by the indicated lattice distortions and rigid body rotation, as follows:

$$r' = [(1-x)\phi_1 B_1 + x\phi_2 B_2]r \quad (20)$$

$$r' = Er \quad (21)$$

$$E = [(1-x)\phi_1 B_1 + x\phi_2 B_2] \quad (22)$$

In this regard, the total distortion matrix, E , can transform any vector in the parent matrix into an internally twinned martensite.

To define the rigid body rotations, ϕ_1 and ϕ_2 cannot be determined from the available data set. However, a rotation ϕ ($\phi_2 = \phi_1\phi$), which gives the relative rotation between ϕ_1 and ϕ_2 , can be defined and the total macroscopic shear can be expressed, as follows:

$$E = \phi_1[(1-x)B_1 + x\phi B_2] = F\phi_1 \quad (23)$$

where $F = (1-x)B_1 + x\phi B_2$.

Therefore, the macroscopic shear taking place during the martensitic transformation contains three components, naming ϕ_1 (i.e. rigid body rotation), F (i.e. the fraction of the shear by the twins) and B_1 (i.e. the Bain strain). For the certain values of x (magnitude of lattice invariant shear, LIS), the matrix produces an eigenvalue problem for the vectors in the habit plane.

Electronic supplementary material: The online version of this article (<https://doi.org/10.1007/s10853-020-05075-7>) contains supplementary material, which is available to authorized users.

References

- [1] Lütjering G, Williams JC (2007) Titanium, 2nd edn. Springer, Berlin
- [2] Lütjering G (2002) Influence of processing on microstructure and mechanical properties of (α + β) titanium alloys. Mater Sci Eng A 243:32–45. [https://doi.org/10.1016/s0921-5093\(97\)00778-8](https://doi.org/10.1016/s0921-5093(97)00778-8)
- [3] Ghonem H (2010) Microstructure and fatigue crack growth mechanisms in high temperature titanium alloys. Int J Fatigue 32:1448–1460. <https://doi.org/10.1016/j.ijfatigue.2010.02.001>
- [4] Serra A, Bacon DJ, Pond RC (2002) Twins as barriers to basal slip in hexagonal-close-packed metals. Met Mater Trans A 33:809–812. <https://doi.org/10.1007/s11661-002-1012-6>
- [5] Wang J, Liu L, Tomé CN et al (2013) Twinning and detwinning via glide and climb of twinning dislocations along serrated coherent twin boundaries in hexagonal-close-packed metals. Mater Res Lett 1:81–88. <https://doi.org/10.1080/21663831.2013.779601>
- [6] Skrotzki W, Wendt H, Carter CB, Kohlstedt DL (1988) The relation between the structure and mechanical properties of a $\Sigma=51$ tilt boundary in germanium. Acta Metall 36:983–994
- [7] Guo Y, Britton TB, Wilkinson AJ (2014) Slip band-grain boundary interactions in commercial-purity titanium. Acta Mater 76:1–12. <https://doi.org/10.1016/j.actamat.2014.05.015>
- [8] Beladi H, Cizek P, Taylor AS et al (2017) Static softening in a Ni-30Fe austenitic model alloy after hot deformation: microstructure and texture evolution. Metall Mater Trans A Phys Metall Mater Sci 48:855–867. <https://doi.org/10.1007/s11661-016-3880-1>
- [9] Kobayashi S, Kobayashi R, Watanabe T (2016) Control of grain boundary connectivity based on fractal analysis for improvement of intergranular corrosion resistance in SUS316L austenitic stainless steel. Acta Mater 102:397–405. <https://doi.org/10.1016/j.actamat.2015.08.075>
- [10] Papillon F, Rohrer GS, Wynblatt P (2009) Effect of segregating impurities on the grain-boundary character distribution of magnesium oxide. J Am Ceram Soc 92:3044–3051. <https://doi.org/10.1111/j.1551-2916.2009.03327.x>
- [11] Pang Y, Wynblatt P (2006) Effects of Nb doping and segregation on the grain boundary plane distribution in TiO 2. J Am Ceram Soc 89:666–671. <https://doi.org/10.1111/j.1551-2916.2005.00759.x>
- [12] Baram M, Chatain D, Kaplan WD (2011) Nanometer-thick equilibrium films: the interface between thermodynamics and atomistics. Science 80(332):206–209. <https://doi.org/10.1126/science.1201596>
- [13] Dillon SJ, Tang M, Carter WC, Harmer MP (2007) Complexion: a new concept for kinetic engineering in materials science. Acta Mater 55:6208–6218. <https://doi.org/10.1016/j.actamat.2007.07.029>
- [14] Beladi H, Nuhfer NT, Rohrer GS (2014) The five-parameter grain boundary character and energy distributions of a fully austenitic high-manganese steel using three dimensional data. Acta Mater 70:281–289. <https://doi.org/10.1016/j.actamat.2014.02.038>
- [15] Beladi H, Rohrer GS (2013) The relative grain boundary area and energy distributions in a ferritic steel determined from three-dimensional electron backscatter diffraction maps. Acta Mater 61:1404–1412. <https://doi.org/10.1016/j.actamat.2012.11.017>

- [16] Haghdadi N, Cizek P, Hodgson PD, He Y, Sun B, Jonas JJ, Rohrer GS, Beladi H (2020) New insights into the interface characteristics of a duplex stainless steel subjected to accelerated ferrite-to-austenite transformation. *J Mater Sci* 55(12):5322–5339
- [17] Kumar M, Schwartz AJ, King WE (2002) Microstructural evolution during grain boundary engineering of low to medium stacking fault energy fcc materials. *Acta Mater* 50:2599–2612. [https://doi.org/10.1016/S1359-6454\(02\)00090-3](https://doi.org/10.1016/S1359-6454(02)00090-3)
- [18] Palumbo G, Lehockey EM, Lin P (1998) Applications for grain boundary engineered materials. *Jom* 50:40–43. <http://doi.org/10.1007/s11837-998-0248-z>
- [19] Schwartz AJ (1998) The potential engineering of grain boundaries through thermomechanical processing. *JOM* 50:50–55. <https://doi.org/10.1007/s11837-998-0250-5>
- [20] Shimada M, Kokawa H, Wang ZJ et al (2002) Optimization of grain boundary character distribution for intergranular corrosion resistant 304 stainless steel by twin-induced grain boundary engineering. *Acta Mater* 50:2331–2341
- [21] Watanabe T (2011) Grain boundary engineering: historical perspective and future prospects. *J Mater Sci* 46:4095–4115. <https://doi.org/10.1007/s10853-011-5393-z>
- [22] Michiuchi M, Kokawa H, Wang ZJ et al (2006) Twin-induced grain boundary engineering for 316 austenitic stainless steel. *Acta Mater* 54:5179–5184. <https://doi.org/10.1016/j.actamat.2006.06.030>
- [23] Haghdadi N, Zarei-Hanzaki A, Farabi E, Cizek P, Beladi H, Hodgson PD (2017) Strain rate dependence of ferrite dynamic restoration mechanism in a duplex low-density steel. *Mater Des* 132:360–366
- [24] Beladi H, Chao Q, Rohrer GS (2014) Variant selection and intervariant crystallographic planes distribution in martensite in a Ti–6Al–4V alloy. *Acta Mater* 80:478–489. <https://doi.org/10.1016/j.actamat.2014.06.064>
- [25] Beladi H, Rohrer GS (2017) The role of thermomechanical routes on the distribution of grain boundary and interface plane orientations in transformed microstructures. *Metall Mater Trans A* 48:2781–2790. <https://doi.org/10.1007/s11661-016-3630-4>
- [26] Randle V (1999) Mechanism of twinning-induced grain boundary engineering in low stacking-fault energy materials. *Acta Mater* 47:4187–4196. [https://doi.org/10.1016/S1359-6454\(99\)00277-3](https://doi.org/10.1016/S1359-6454(99)00277-3)
- [27] Haghdadi N, Cizek P, Hodgson PD et al (2018) Effect of ferrite-to-austenite phase transformation path on the interface crystallographic character distributions in a duplex stainless steel. *Acta Mater* 145:196–209. <https://doi.org/10.1016/j.actamat.2017.11.057>
- [28] Haghdadi N, Cizek P, Hodgson PD et al (2018) Five-parameter crystallographic characteristics of the interfaces formed during ferrite to austenite transformation in a duplex stainless steel. *Philos Mag* 98:1284–1306. <https://doi.org/10.1080/14786435.2018.1434321>
- [29] Beladi H, Rohrer GS (2013) The distribution of grain boundary planes in interstitial free steel. *Metall Mater Trans A Phys Metall Mater Sci* 44:115–124. <https://doi.org/10.1007/s11661-012-1393-0>
- [30] Beladi H, Tari V, Timokhina IB et al (2017) On the crystallographic characteristics of nanobainitic steel. *Acta Mater* 127:426–437. <https://doi.org/10.1016/j.actamat.2017.01.058>
- [31] Beladi H, Rohrer GS, Rollett AD et al (2014) The distribution of intervariant crystallographic planes in a lath martensite using five macroscopic parameters. *Acta Mater* 63:86–98. <https://doi.org/10.1016/j.actamat.2013.10.010>
- [32] Hutchinson B, Komenda J, Rohrer GS, Beladi H (2015) Heat affected zone microstructures and their influence on toughness in two microalloyed HSLA steels. *Acta Mater* 97:380–391. <https://doi.org/10.1016/j.actamat.2015.05.055>
- [33] Wang SC, Aindow M, Starink MJ (2003) Effect of self-accommodation on α/α boundary populations in pure titanium. *Acta Mater* 51:2485–2503. [https://doi.org/10.1016/S1359-6454\(03\)00035-1](https://doi.org/10.1016/S1359-6454(03)00035-1)
- [34] Farabi E, Hodgson PD, Rohrer GS, Beladi H (2018) Five-parameter intervariant boundary characterization of martensite in commercially pure titanium. *Acta Mater* 154:147–160. <https://doi.org/10.1016/j.actamat.2018.05.023>
- [35] Burgers WGG (1934) On the process of transition of the cubic-body-centered modification into the hexagonal-close-packed modification of zirconium. *Physica* 1:561–586. [http://doi.org/10.1016/S0031-8914\(34\)80244-3](http://doi.org/10.1016/S0031-8914(34)80244-3)
- [36] Qiu D, Shi R, Zhao P et al (2016) Effect of low-angle grain boundaries on morphology and variant selection of grain boundary allotriomorphs and Widmanstätten side-plates. *Acta Mater* 112:347–360. <https://doi.org/10.1016/j.actamat.2016.04.033>
- [37] Shi R, Dixit V, Fraser HL, Wang Y (2014) Variant selection of grain boundary α by special prior β grain boundaries in titanium alloys. *Acta Mater* 75:156–166. <https://doi.org/10.1016/j.actamat.2014.05.003>
- [38] Qiu D, Shi R, Zhang D et al (2015) Variant selection by dislocations during α precipitation in α/β titanium alloys. *Acta Mater* 88:218–231. <https://doi.org/10.1016/j.actamat.2014.12.044>
- [39] Shi R, Dixit V, Viswanathan GB et al (2016) Experimental assessment of variant selection rules for grain boundary α in titanium alloys. *Acta Mater* 102:197–211. <https://doi.org/10.1016/j.actamat.2015.09.021>

- [40] Banerjee S, Mukhopadhyay P (2007) Martensitic transformations. In: Phase transformations: examples from titanium and zirconium Alloys, first ed. Elsevier, pp 259–376
- [41] Balachandran S, Kashiwar A, Choudhury A et al (2016) On variant distribution and coarsening behavior of the α phase in a metastable β titanium alloy. *Acta Mater* 106:374–387. <https://doi.org/10.1016/j.actamat.2016.01.023>
- [42] Williams AJ, Cahn RW, Barrett CS (1954) The crystallography of the β - α transformation in titanium. *Acta Metall* 2:117–128. [https://doi.org/10.1016/0001-6160\(54\)90101-7](https://doi.org/10.1016/0001-6160(54)90101-7)
- [43] Hua K, Zhang Y, Gan W et al (2018) Correlation between imposed deformation and transformation lattice strain on α variant selection in a metastable β -Ti alloy under isothermal compression. *Acta Mater* 161:150–160. <https://doi.org/10.1016/j.actamat.2018.09.022>
- [44] Khundzhua AG, Ptitsyn AG, Brovkina EA, Chzhen S (2012) Self-accommodation of crystals of martensitic phases in titanium and zirconium based alloys. *Phys Met Metallogr* 113:1035–1040. <https://doi.org/10.1134/s0031918x12110117>
- [45] Nishida M, Nishiura T, Kawano H, Inamura T (2012) Self-accommodation of B19' martensite in Ti–Ni shape memory alloys—Part I. Morphological and crystallographic studies of the variant selection rule. *Philos Mag* 92:2215–2233. <http://doi.org/10.1080/14786435.2012.669858>
- [46] Miyazaki S, Otsuka K, Wayman CM (1989) The shape memory mechanism associated with the martensitic transformation in TiNi alloys-I. Self-Accomm *Acta Metall* 37:1873–1884. [https://doi.org/10.1016/0001-6160\(89\)90072-2](https://doi.org/10.1016/0001-6160(89)90072-2)
- [47] Srivastava D, Madangopal K, Banerjee S, Ranganathan S (1993) Self accommodation morphology of martensite variants in Zr-2.5wt % Nb alloy. *Acta Metall Mater* 41:3445–3454
- [48] Germain L, Gey N, Humbert M et al (2005) Analysis of sharp microtexture heterogeneities in a bimodal IMI 834 billet. *Acta Mater* 53:3535–3543. <https://doi.org/10.1016/j.actamat.2005.03.043>
- [49] Humbert M, Germain L, Gey N et al (2006) Study of the variant selection in sharp textured regions of bimodal IMI 834 billet. *Mater Sci Eng A* 430:157–164. <https://doi.org/10.1016/j.msea.2006.05.047>
- [50] Divinski SV, Dnieprenko VN, Ivasishin OM (1998) Effect of phase transformation on texture formation in Ti-base alloys. *Mater Sci Eng A* 243:201–205
- [51] Qiu D, Zhao P, Shi R et al (2016) Effect of autocatalysis on variant selection of α precipitates during phase transformation in Ti–6Al–4V alloy. *Comput Mater Sci* 124:282–289. <https://doi.org/10.1016/j.commatsci.2016.07.032>
- [52] Lieberman DS (1958) Martensitic transformations and determination of the inhomogeneous deformation. *Acta Metall* 6:680–693. [https://doi.org/10.1016/0001-6160\(58\)90059-2](https://doi.org/10.1016/0001-6160(58)90059-2)
- [53] Lieberman DS, Wechsler MS, Read TA (1955) Cubic to orthorhombic diffusionless phase change—experimental and theoretical studies of AuCd. *J Appl Phys* 26:473–484
- [54] Wayman CM (1964) Introduction to the crystallography of martensitic transformations. Macmillan, Newyork
- [55] Saylor DM, El-Dasher BS, Adams BL, Rohrer GS (2004) Measuring the five-parameter grain-boundary distribution from observations of planar sections. *Metall Mater Trans A* 35:1981–1989. <https://doi.org/10.1007/s11661-004-0147-z>
- [56] Rohrer GS, Saylor DM, El Dasher B et al (2004) The distribution of internal interfaces in polycrystals. *Zeitschrift für Met* 95:197–214. <https://doi.org/10.3139/146.017934>
- [57] Ratanaphan S, Yoon Y, Rohrer GS (2014) The five parameter grain boundary character distribution of polycrystalline silicon. *J Mater Sci* 49:4938–4945. <https://doi.org/10.1007/s10853-014-8195-2>
- [58] Gey N, Humbert M (2002) Characterization of the variant selection occurring during the α to β phase transformations of a cold rolled titanium sheet. *Acta Mater* 50:277–287. [https://doi.org/10.1016/S1359-6454\(01\)00351-2](https://doi.org/10.1016/S1359-6454(01)00351-2)
- [59] Wang J, Beyerlein IJ (2012) Atomic structures of symmetric tilt grain boundaries in Hexagonal Close-Packed (hcp) crystals. *Metall Mater Trans A Phys Metall Mater Sci* 20:1–22. <https://doi.org/10.1088/0965-0393/20/2/024002>
- [60] Glowinski K, Morawiec A (2012) A toolbox for geometric grain boundary characterization. In: Proceedings of the 1st international conference on 3d materials science. Springer, Cham, pp 119–124
- [61] Otsuka K, Wayman CM (1999) Shape memory materials. Cambridge University Press, Cambridge
- [62] Banerjee S, Mukhopadhyay P (2010) Phase transformations: examples from titanium and zirconium alloys. Elsevier, Amsterdam
- [63] Zhang Y, Li Z, Esling C et al (2010) A general method to determine twinning elements. *J Appl Crystallogr* 43:1426–1430. <https://doi.org/10.1107/S0021889810037180>
- [64] Bilby BA, Crocker AG (1965) The theory of the crystallography of deformation twinning. *Proc R Soc A Math Phys Eng Sci* 288:240–255
- [65] Hammond C, Kelly P (1969) The crystallography of titanium alloy martensites. *Acta Metall* 17:869–882. [https://doi.org/10.1016/0001-6160\(69\)90107-2](https://doi.org/10.1016/0001-6160(69)90107-2)
- [66] Nishiyama Z, Oka M, Nakagawa H (1965) 10–11 transformation twins in titanium. *Jpn Inst Met* 7:1–4
- [67] Grabovetskaya GP, Melnikova EN, Kolobov YR et al (2006) Evolution of the structural and phase states of a Ti–6Al–4V

- alloy in forming submicrocrystalline structure with the use of temporary hydrogenation. *Russ Phys J* 49:442–447. <https://doi.org/10.1007/s11182-006-0123-8>
- [68] Swarnakar AK, Van Der Biest O, Baufeld B (2011) Thermal expansion and lattice parameters of shaped metal deposited Ti–6Al–4V. *J Alloys Compd* 509:2723–2728. <https://doi.org/10.1016/j.jallcom.2010.12.014>
- [69] Shibata M, Ono K (1977) On the minimization of strain energy in the martensitic transformation of titanium. *Acta Metall* 25:35–42. [https://doi.org/10.1016/0001-6160\(77\)90243-7](https://doi.org/10.1016/0001-6160(77)90243-7)
- [70] Morawiec A (2012) On “interface-plane scheme” and symmetric grain boundaries. *Zeitschrift fur Krist* 227:199–206. <https://doi.org/10.1524/zkri.2012.1475>
- [71] Randle V (2010) Role of grain boundary plane in grain boundary engineering. *Mater Sci Technol* 26:774–780. <https://doi.org/10.1179/026708309X12567268926641>
- [72] Randle V (2010) Grain boundary engineering: an overview after 25 years. *Mater Sci Technol* 26:253–261. <https://doi.org/10.1179/026708309X1260195277747>
- [73] Randle V (2004) Twinning-related grain boundary engineering. *Acta Mater* 52:4067–4081. <https://doi.org/10.1016/j.actamat.2004.05.031>
- [74] Gruber J, George DC, Kuprat AP et al (2005) Effect of anisotropic grain boundary properties on grain boundary plane distributions during grain growth. *Scr Mater* 53:351–355. <https://doi.org/10.1016/j.scriptamat.2005.04.004>
- [75] Gruber J, Miller HM, Hoffmann TD et al (2009) Misorientation texture development during grain growth. Part I: Simulation and experiment. *Acta Mater* 57:6102–6112. <https://doi.org/10.1016/j.actamat.2009.08.036>
- [76] Ratanaphan S, Olmsted DL, Bulatov VV et al (2015) Grain boundary energies in body-centered cubic metals. *Acta Mater* 88:346–354. <https://doi.org/10.1016/j.actamat.2015.01.069>
- [77] Dillon SJ, Rohrer GS (2009) Mechanism for the development of anisotropic grain boundary character distributions during normal grain growth. *Acta Mater* 57:1–7. <https://doi.org/10.1016/j.actamat.2008.08.062>
- [78] Li J, Dillon SJ, Rohrer GS (2009) Relative grain boundary area and energy distributions in nickel. *Acta Mater* 57:4304–4311. <https://doi.org/10.1016/j.actamat.2009.06.004>
- [79] Rohrer GS, Li J, Lee S et al (2010) Deriving grain boundary character distributions and relative grain boundary energies from three-dimensional EBSD data. *Mater Sci Technol* 26:661–669. <https://doi.org/10.1179/026708309X12468927349370>
- [80] Sutton AP (1991) An analytic model for grain-boundary expansions and cleavage energies. *Philos Mag A* 63:793–818
- [81] Wolf D (1990) Correlation between structure, energy, and ideal cleavage fracture for symmetrical grain boundaries in fcc metals. *J Mater Res* 5:1708–1730. [https://doi.org/10.1016/0036-9748\(89\)90482-1](https://doi.org/10.1016/0036-9748(89)90482-1)
- [82] Fan Q (2012) A new method of calculating interplanar spacing: The position-factor method. *J Appl Crystallogr* 45:1303–1308. <https://doi.org/10.1107/S0021889812037764>
- [83] Wang J, Beyerlein IJ (2012) Atomic structures of symmetric tilt grain boundaries in hexagonal close packed (hcp) crystals. *Model Simul Mater Sci Eng* 20:24002. <https://doi.org/10.1088/0965-0393/20/2/024002>
- [84] Greninger AB, Troiano AR (1940) Crystallography of austenite decomposition. *Trans AIME* 140:307–336
- [85] Mackenzie J, Bowles J (1954) The crystallography of martensite transformations II. *Acta Metall* 2:138–147. [https://doi.org/10.1016/0001-6160\(54\)90103-0](https://doi.org/10.1016/0001-6160(54)90103-0)
- [86] Bowles JS, Mackenzie JK (1954) The crystallography of martensite transformations I. *Acta Mater* 2:129–137. [https://doi.org/10.1016/0001-6160\(54\)90102-9](https://doi.org/10.1016/0001-6160(54)90102-9)
- [87] Bhadeshia HKDH (2001) Worked examples in the Geometry of Crystals, 2nd edn. The Institute of Metals, London

Publisher's Note Springer Nature remains neutral with regard to jurisdictional claims in published maps and institutional affiliations.